

Intervalence Charge Transfer Luminescence: The Anomalous Luminescence of Cerium-Doped $\text{Cs}_2\text{LiLuCl}_6$ Elpasolite.

Luis Seijo^{1,2} and Zoila Barandiarán^{1,2}

¹Departamento de Química, Universidad Autónoma de Madrid, 28049 Madrid, Spain

²Instituto Universitario de Ciencia de Materiales Nicolás Cabrera,

Universidad Autónoma de Madrid, 28049 Madrid, Spain

(Dated: March 22, 2022)

The existence of intervalence charge transfer (IVCT) luminescence is reported. It is shown that the so called anomalous luminescence of Ce-doped elpasolite $\text{Cs}_2\text{LiLuCl}_6$, which is characterized mainly by a very large Stokes shift and a very large band width, corresponds to an IVCT emission that takes place in Ce^{3+} - Ce^{4+} pairs, from the $5d_{e_g}$ orbital of Ce^{3+} to $4f$ orbitals of Ce^{4+} . Its Stokes shift is the sum of the large reorganization energies of the Ce^{4+} and Ce^{3+} centers formed after the fixed-nuclei electron transfer and it is equal to the energy of the IVCT absorption commonly found in mixed-valence compounds, which is predicted to exist in this material and to be slightly larger than 10000 cm^{-1} . The large band width is the consequence of the large offset between the minima of the Ce^{3+} - Ce^{4+} and Ce^{4+} - Ce^{3+} pairs along the electron transfer reaction coordinate. This offset is approximately $2\sqrt{3}$ times the difference of Ce-Cl equilibrium distances in the Ce^{3+} and Ce^{4+} centers. It is shown that the energies of the peaks and the widths of IVCT absorption and emission bands can be calculated *ab initio* with reasonable accuracy from diabatic energy surfaces of the ground and excited states and that these can be obtained, in turn, from independent calculations on the donor and acceptor active centers. We obtained the energies of the Ce^{3+} and Ce^{4+} active centers of Ce-doped $\text{Cs}_2\text{LiLuCl}_6$ by means of state-of-the-art wave-function-theory spin-orbit coupling relativistic calculations on the donor cluster $(\text{CeCl}_6\text{Li}_6\text{Cs}_8)^{11+}$ and the acceptor cluster $(\text{CeCl}_6\text{Li}_6\text{Cs}_8)^{12+}$ embedded in a quantum mechanical embedding potential of the host. The calculations provide interpretations of unexplained experimental observations as due to higher energy IVCT absorptions, and allow to reinterpret others. The existence of another IVCT emission of lower energy, at around 14000 - 16000 cm^{-1} less than the $5d_{t_{2g}}$ emission, is also predicted.

Keywords: *Ab initio*, IVCT, electron transfer, Ce^{3+} , Ce^{4+} , intermetallic pairs, mixed valence, diabatic

I. INTRODUCTION

Intervalence charge transfer (IVCT) is the conventional name for electron transfer between two metal sites differing only in oxidation state.¹ Therefore, it is a particular case of metal-to-metal charge transfer (MMCT) in which the two metal ions involved in the redox process are identical; in other words, it is the homonuclear, symmetric MMCT.² The basic theory for electron transfer was formulated by Marcus³ and the systematic study of intervalence compounds^{4,5} has played a key role in elucidating electron transfer reactions. The electron transfer between the ground states of the two metal sites can be thermally induced after passing through an activated complex with an activation energy barrier; in the activated complex the electron is equally distributed among the two metallic centers. The electron transfer can also be photoinduced. In this case, a fixed nuclei IVCT photon absorption takes place that is followed by a nonradiative decay involving nuclei reorganization; the decay passes through the activated complex and it can branch either to the original state or to the charge transfer state, which are degenerate (Fig. 1, red lines). Obviously, there cannot be any emission associated with the IVCT absorption. IVCT absorption explained the early observations of Werner⁶ on the dark color of substances containing platinum in two oxidation states and it was found in a large number of mixed valence compounds,^{4,5} mostly involving transition metals. The Marcus theory of elec-

tron transfer was complemented by Hush^{7,8} with a theory of heteronuclear MMCT and homonuclear IVCT considering a two-state problem. Piepho *et al.*⁹ formulated a vibronic model for the IVCT absorption of the two-state problem. We are not aware of extensions of these theories to absorptions and emissions involving higher excited states of the mixed valence compounds.

The relevance of MMCT transitions in solids has been reviewed by Blasse,¹⁰ including IVCT absorptions in mixed-valence compounds; most of the materials involve transition metal ions. In f-element doped solids, MMCT between f-elements and the cations of the host have been considered responsible for green-blue luminescence quenching and red luminescence induction in Pr^{3+} -doped compounds,¹¹ and a near-IR/Visible broad absorption band in Ce-doped LaPO_4 has been ascribed to a Ce^{3+} - Ce^{4+} IVCT absorption,¹² for instance, but neither heteronuclear MMCT nor homonuclear IVCT have been the subject of extensive investigations.

Although the IVCT absorption is very well known in mixed valence compounds, IVCT luminescence transitions (Fig. 1 blue arrow) have never been reported, to the best of our knowledge. A series of *ab initio* studies on lanthanide optically active centers in solids is leading us to propose that IVCT emissions have in fact been observed in Ce-doped elpasolites and in Yb-doped fluorites, even though they have not been identified as such. We also expect these emissions to be present in Eu-doped solids and in other solids doped with f-elements in which several valence states are likely to coexist. IVCT states are also likely to be respon-

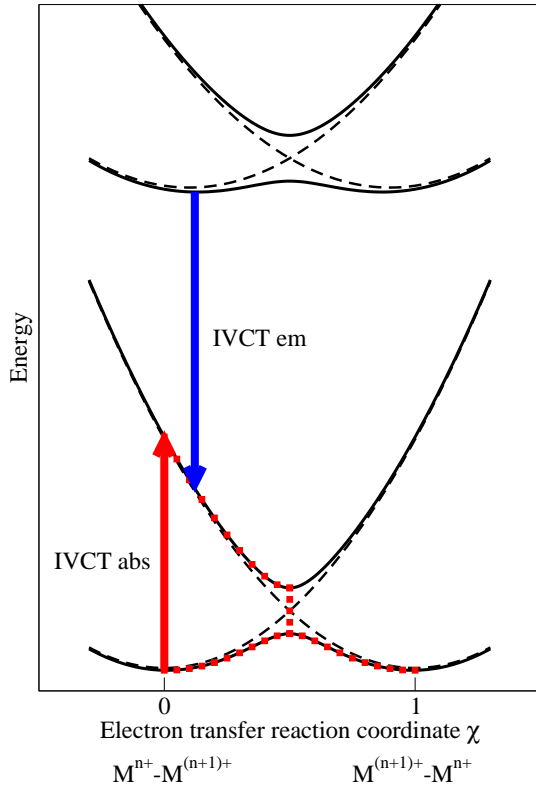


FIG. 1: Schematic representation of an intervalence charge transfer absorption (red arrow) and emission (blue arrow), followed by nonradiative decay (red squares). Diabatic (dashed lines) and adiabatic (full lines) energy curves of the ground and excited states of the $M^{n+}-M^{(n+1)+}$ and $M^{(n+1)+}-M^{n+}$ pairs are shown.

sible for luminescence quenching in many materials. Here we report *ab initio* calculations on the IVCT luminescence of Ce-doped $\text{Cs}_2\text{LiLuCl}_6$. In a separate paper we report *ab initio* calculations on the IVCT luminescence of Yb-doped fluorites.¹³

Ce-doped $\text{Cs}_2\text{LiLuCl}_6$ elpasolite is a scintillating material that presents an anomalous luminescence.¹⁴ Such emission is excited by the $4f \rightarrow 5de_g$ absorption but it cannot be a usual $5de_g \rightarrow 4f$ emission because its energy is much lower than its excitation (more than 9000 cm^{-1} lower) and its band width is very large (full width at half maximum of 4800 cm^{-1} at room temperature). Its intensity increases with temperature up to 250 K and decreases above it. This anomalous luminescence was also found in $\text{Cs}_3\text{LuCl}_6:\text{Ce}$ [Ref. 15] and $\text{Cs}_2\text{NaYCl}_6:\text{Ce}$ [Ref. 16]; in these materials it is quenched at room temperature but the basic mechanism is likely to be the same in all three.

In this work, we interpret the anomalous luminescence of $\text{Cs}_2\text{LiLuCl}_6:\text{Ce}$ as a $\text{Ce}^{3+} 5de_g \rightarrow \text{Ce}^{4+} 4f$ intervalence charge transfer emission that takes place in $\text{Ce}^{3+}-\text{Ce}^{4+}$ active pairs. This interpretation is based on wave function theory *ab initio* calculations on Ce-doped $\text{Cs}_2\text{LiLuCl}_6$ which involve: the $4f^1$ and $5d^1$ manifolds of the Ce^{3+} active center, and its a_{1g}^1 impurity-trapped exciton (ITE); the Ce^{4+} closed-shell center; and the diabatic energy surfaces of the

$\text{Ce}^{3+}-\text{Ce}^{4+}$ active pair along the electron transfer reaction coordinates of the ground state and excited states.

The results suggest that $\text{Ce}^{3+}-\text{Ce}^{4+}$ IVCT states might also be responsible for other not well understood features of related materials, like unassigned low-T excitation bands of $\text{Cs}_2\text{NaYCl}_6:\text{Ce}$ [Ref. 17] and $\text{Cs}_2\text{NaYF}_6:\text{Ce}$ [Ref. 18], and the anomalous behaviour of the 351 nm emission of $\text{Cs}_2\text{NaYF}_6:\text{Ce}$ under various excitation wavelengths.¹⁸

Also, it is shown that the diabatic energy surfaces of the $\text{Ce}^{3+}-\text{Ce}^{4+}$ mixed valence pairs are sufficient to provide the basic understanding of the states involved in the relevant absorptions, emissions, and nonradiative decays. They can be obtained from independent *ab initio* calculations in embedded monometallic clusters of the oxidized and reduced species, like $(\text{CeCl}_6)^{3-}$ and $(\text{CeCl}_6)^{2-}$. The adiabatic energy surfaces, which require much more demanding calculations on embedded dimetallic clusters like $(\text{Ce}_2\text{Cl}_{12})^{5-}$, are only necessary when electronic interaction between them are expected to be significant and accurate numerical results are targeted.

II. POTENTIAL ENERGY SURFACES OF MIXED VALENCE ACTIVE PAIRS

The intervalence charge transfer luminescence of Ce-doped $\text{Cs}_2\text{LiLuCl}_6$ takes place between states of $\text{Ce}^{3+}-\text{Ce}^{4+}$ mixed valence active pairs. In Secs. II A and II B we describe the basics of their adiabatic and diabatic potential energy surfaces (equivalent to the full and dashed lines in Fig. 1, respectively) and their relations.

A. Adiabatic potential energy surfaces

Let us consider a *donor* D and an *acceptor* A , which in this case will be the separated embedded clusters $(\text{CeCl}_6)^{3-}$ and $(\text{CeCl}_6)^{2-}$. Let us also consider a *donor-acceptor* pair prior to electron transfer, DA , and after the electron transfer, D^+A^- . In the homonuclear, symmetric MMCT case, or IVCT, D^+ is A and A^- is D , so that we can call the pair after the electron transfer the *acceptor-donor* pair AD . In this case, DA and AD will be the mixed valence embedded cluster $(\text{Ce}_2\text{Cl}_{12})^{5-}$ with conventional left-right distributions $\text{Ce}^{3+}-\text{Ce}^{4+}$ and $\text{Ce}^{4+}-\text{Ce}^{3+}$ respectively. We are interested in the energies of the DA and AD pairs in their ground and excited states as functions of the nuclear coordinates. Since the electronic spectroscopic transitions are dominated by the totally symmetric vibrational coordinates, we will only consider the breathing modes of octahedral $(\text{CeCl}_6)^{3-}$ and $(\text{CeCl}_6)^{2-}$, so that the only vibrational degrees of freedom will be the Ce-Cl distances in the left and right components of the pairs, d_L and d_R . For each nuclear configuration, the electronic states of the pairs result from the combinations between the n_D individual states of D and the n_A individual states of A . In this case they will be the states of the $4f^1$, $5dt_{2g}^1$, $5de_g^1$, and $a_{1g,ITE}^1$ (impurity-trapped exciton) configurations of $(\text{CeCl}_6)^{3-}$ combined with the A_{1g}

closed-shell state of $(\text{CeCl}_6)^{2-}$. Besides, since both DA and AD electronic configurations are possible, the total number of adiabatic electronic states Φ_k of the mixed valence pair is $2n_D n_A$. Their adiabatic potential energy surfaces (equivalent to the full lines in Fig. 1) will be $E_k(d_L, d_R)$, $k = 1, 2, \dots, 2n_D n_A$. These adiabatic energy surfaces can provide basic spectroscopic data without requiring to solve the full vibronic problem, like the positions of absorption and emission band maxima via the Frank-Condon approximation, and others. In general, they result from direct quantum mechanical calculations on mixed valence dimers, which are highly demanding. Depending on the number of open-shell electrons of the lanthanide, they can be extremely demanding.

B. Diabatic potential energy surfaces

1. Definition

Independently of the method used for the calculation of the adiabatic potential energy surfaces, they can be considered to result from the diagonalization of a $(2n_D n_A \times 2n_D n_A)$ interaction matrix. The diagonal elements of the interaction matrix are the diabatic potential energy surfaces (equivalent to the dashed lines in Fig. 1) and the off-diagonal elements are the electronic couplings. The diabatic energy surfaces can cross each other and, contrary to the adiabatic, they maintain the nature of the electronic state across the crossings. The diabatic basis is arbitrary; a convenient choice is the set of generalized antisymmetric product functions^{19,20} resulting from the combination of the states of D and A . So, from the combination of the i state of D , Φ_{Di} , and the j state of A , Φ_{Aj} , we will have two diabatic wavefunctions: one for the ij state of DA , $M\hat{A}(\Phi_{Di}\Phi_{Aj})$, and one for the ji state of AD , $M\hat{A}(\Phi_{Aj}\Phi_{Di})$ (M is a normalization constant and \hat{A} is the inter-group antisymmetrization operator¹⁹). Their expected values of the fixed nuclei Hamiltonian of the embedded pair \hat{H} , are the two corresponding diabatic potential energy surfaces $E_{DiAj}^{\text{diab}}(d_L, d_R)$ and $E_{AjDi}^{\text{diab}}(d_L, d_R)$: $E_{DiAj}^{\text{diab}} = \langle M\hat{A}(\Phi_{Di}\Phi_{Aj}) | \hat{H} | M\hat{A}(\Phi_{Di}\Phi_{Aj}) \rangle$, $E_{AjDi}^{\text{diab}} = \langle M\hat{A}(\Phi_{Aj}\Phi_{Di}) | \hat{H} | M\hat{A}(\Phi_{Aj}\Phi_{Di}) \rangle$. Their electronic coupling is $V_{DiAj,AjDi}^{\text{diab}} = \langle M\hat{A}(\Phi_{Di}\Phi_{Aj}) | \hat{H} | M\hat{A}(\Phi_{Aj}\Phi_{Di}) \rangle$. Note that $E_{DiAj}^{\text{diab}}(x, y) = E_{AjDi}^{\text{diab}}(y, x)$.

We must remark now that, if the full vibronic problem of the mixed valence pair needed to be solved, both the adiabatic basis $\{\Phi_k\}$ and the diabatic basis $\{M\hat{A}(\Phi_{Di}\Phi_{Aj}), M\hat{A}(\Phi_{Aj}\Phi_{Di})\}$, would be valid alternatives leading to the same vibronic energies and wavefunctions. If, instead, the focus is on some relevant features of the electronic spectra like zero-phonon lines, absorption and emission band maxima and band widths, etc., or of the electronic states of the mixed valence pair, like equilibrium structures, activation energy barriers, etc., the adiabatic energy surfaces are the valid ones and the diabatic energy sur-

faces are an approximation to them. Let us briefly discuss on the limits of the diabatic approximation.

In the regions of the nuclear configuration space where the electronic couplings are not very large, the adiabatic and diabatic energy surfaces are close, each adiabatic wavefunction Φ_k is very similar to one of the diabatic wavefunctions, and a particular $D_i A_j$ or $A_j D_i$ character can be associated with it. E.g., for d_L and d_R values respectively close to the Ce-Cl equilibrium distance of the Ce^{3+} donor site and of the Ce^{4+} acceptor site, one of the adiabatic energies will be close to E_{DiAj}^{diab} and another to E_{AjDi}^{diab} ; E_{DiAj}^{diab} will be the lowest of the two because both the donor and the acceptor are structurally relaxed, and E_{AjDi}^{diab} will be the highest of the two because both the donor and the acceptor are structurally stressed, each of them being in the equilibrium structure of the other. This is an important observation because the calculations of the diabatic energy surfaces, which can be highly demanding, are always significantly less demanding than the calculations of the adiabatic ones.

In the regions of the nuclear configuration space near crossings of diabatic energy surfaces, e.g. near the activated complex where $d_L \approx d_R$, the electronic couplings have larger effects and produce avoided crossings. The crossing diabatic states are then replaced by a lower adiabatic state with a smaller thermal energy barrier, plus an upper adiabatic state which has become stable at the configuration where the electron is equally distributed among the two metals (see Fig. 1). In these regions, the adiabatic results are necessary when quantitative energy barriers or quantitative nonradiative dynamics are targeted. Many of the spectroscopic features of the mixed valence pairs can however be addressed quantitatively or semiquantitatively with the diabatic energy surfaces only. We describe next how they can be computed.

2. Approximations

The diabatic pair energies are the sum of the donor and acceptor energies plus their mutual Coulomb and exchange interaction.²⁰ The latter should be almost independent of the donor and acceptor states, in general. Hence, we can write:

$$E_{DiAj}^{\text{diab}} = E_{Di} + E_{Aj} + E_{DiAj}^{\text{cx}} \approx E_{Di} + E_{Aj} + E_{DA}^{\text{cx}}. \quad (1)$$

In Eq. 1, E_{Di} and E_{Aj} include the embedding interactions of D and A with the crystalline environment of the DA pair in $\text{Cs}_2\text{LiLuCl}_6$. We aim at computing E_{DiAj}^{diab} by means of embedded cluster calculations and we can think of two alternative computational strategies: In one of them, the symmetry reductions around D and A due to the presence of the other (A and D respectively) are considered from the very beginning. In the other, they are removed in a first step and they are considered later, at the same time that the electronic couplings, i.e. when the adiabatic surfaces are calculated. The strength of the first approach is to be able to give energy splittings driven by symmetry lowering, which are dependent on the distance and relative orientation between

D and A . The strength of the second approach is to be able to give the basics of the energy surfaces by means of independent calculations on the embedded D and A . These alternatives are as follows:

1) One calculation **1D** of the donor (CeCl₆)³⁻ embedded in a Cs₂LiLuCl₆ lattice in which one Lu³⁺ ion is substituted by a Ce⁴⁺ ion gives $E_{Di}^{(1)} = E_{Di} + E_{DA}^{cx}$. Another calculation **1A** of the acceptor (CeCl₆)²⁻ embedded in a Cs₂LiLuCl₆ lattice in which one Lu³⁺ ion is substituted by a Ce³⁺ ion gives $E_{Aj}^{(1)} = E_{Aj} + E_{DA}^{cx}$. Then, $E_{DiAj}^{diab} = E_{Di}^{(1)} + E_{Aj}^{(1)} - E_{DA}^{cx}$. Here, $E_{Di}^{(1)}$ and $E_{Aj}^{(1)}$ depend on the relative positions of D and A . E_{DA}^{cx} is dominated by the long-range Coulomb interactions, so that, except for short donor-acceptor distances, $E_{DA}^{cx} \approx -(q_D \times q_A)e^2/d_{DA} = -(3 \times 4)e^2/d_{DA}$. According to this alternative we have:

$$\begin{aligned} E_{DiAj}^{diab}(d_L, d_R) &= E_{Di}^{(1)}(d_L) + E_{Aj}^{(1)}(d_R) + \Delta E_1^{cx}(d_{DA}), \\ E_{AjDi}^{diab}(d_L, d_R) &= E_{Aj}^{(1)}(d_L) + E_{Di}^{(1)}(d_R) + \Delta E_1^{cx}(d_{DA}), \end{aligned} \quad (2)$$

with

$$\Delta E_1^{cx}(d_{DA}) = -E_{DA}^{cx}(d_{DA}) \approx -(q_D \times q_A)e^2/d_{DA}. \quad (3)$$

2) One calculation **2D** of the donor (CeCl₆)³⁻ embedded in a Cs₂LiLuCl₆ lattice gives $E_{Di}^{(2)} = E_{Di} + E_{DC}^{cx}$, where E_{DC}^{cx} stands for the Coulomb and exchange interaction energy between the donor (CeCl₆)³⁻ and the cluster with the original host cation C (Lu³⁺ in this case), (LuCl₆)³⁻. Another calculation **2A** of the acceptor (CeCl₆)²⁻ embedded in a Cs₂LiLuCl₆ lattice gives $E_{Aj}^{(2)} = E_{Aj} + E_{AC}^{cx}$, where E_{AC}^{cx} stands for the Coulomb and exchange interaction energy between the acceptor (CeCl₆)²⁻ and the cluster with the original host cation, (LuCl₆)³⁻. Then, $E_{DiAj}^{diab} = E_{Di}^{(2)} + E_{Aj}^{(2)} - E_{DC}^{cx} - E_{AC}^{cx} + E_{DA}^{cx}$. Here, $E_{Di}^{(2)}$ and $E_{Aj}^{(2)}$ are independent of the relative positions of D and A . Except for short cation-cation distances, $-E_{DC}^{cx} - E_{AC}^{cx} + E_{DA}^{cx} \approx (-q_D \times q_C - q_A \times q_C + q_D \times q_A)e^2/d_{DA} = (-3 \times 3 - 4 \times 3 + 3 \times 4)e^2/d_{DA} = -(3 \times 3)e^2/d_{DA}$. According to this alternative we have:

$$\begin{aligned} E_{DiAj}^{diab}(d_L, d_R) &= E_{Di}^{(2)}(d_L) + E_{Aj}^{(2)}(d_R) + \Delta E_2^{cx}(d_{DA}), \\ E_{AjDi}^{diab}(d_L, d_R) &= E_{Aj}^{(2)}(d_L) + E_{Di}^{(2)}(d_R) + \Delta E_2^{cx}(d_{DA}), \end{aligned} \quad (4)$$

with

$$\begin{aligned} \Delta E_2^{cx}(d_{DA}) &= E_{DA}^{cx}(d_{DA}) - E_{DC}^{cx}(d_{DA}) - E_{AC}^{cx}(d_{DA}) \\ &\approx (q_D \times q_A - (q_D + q_A) \times q_C)e^2/d_{DA}. \end{aligned} \quad (5)$$

Summarizing, the diabatic potential energy surfaces will be given by:

$$\begin{aligned} E_{DiAj}^{diab}(d_L, d_R) &= E_{Di}(d_L) + E_{Aj}(d_R) + E_0(d_{DA}), \\ E_{AjDi}^{diab}(d_L, d_R) &= E_{Aj}(d_L) + E_{Di}(d_R) + E_0(d_{DA}), \end{aligned} \quad (6)$$

with donor and acceptor energies E_{Di} and E_{Aj} obtained in embedded cluster calculations **1D** and **1A** and the term E_0 ,

which is common to the AD and DA energy surfaces, given by Eq. 3 (alternative 1), or with donor and acceptor energies obtained in embedded cluster calculations **2D** and **2A** and the common term E_0 given by Eq. 5 (alternative 2). Alternative 1 has into account the effects of charge substitutions in the original lattice on the energy levels of D and A . In the present case, the most important ones are expected to be the splittings produced on the (CeCl₆)³⁻ levels. They should be responsible for fine features of the spectra, but not for the number and positions of the main absorption and emission bands. In any case, this alternative implies site symmetry reduction, which may add significant computational effort. Alternative 2 neglects these effects. It has, however, an important computational advantage: the diabatic potential energy surfaces of the mixed valence pairs are computed using the energy curves of the donor and acceptor centers embedded in the original host lattice, i.e. of the clusters (CeCl₆)³⁻ and (CeCl₆)²⁻ embedded in Cs₂LiLuCl₆ in our case. We must remark that, regardless of the alternative used, the term $E_0(d_{DA})$ is common to the DA and AD energy surfaces and to all states of both. Its effect is a common shift of all of them and, consequently, it does not contribute to energy differences between them. In this work we have adopted alternative 2.

3. Topology

The diabatic potential energy surfaces of the DA and AD mixed valence pairs in their ground states, $E_{D0A0}^{diab}(d_L, d_R)$ and $E_{A0D0}^{diab}(d_L, d_R)$, are shown in Fig. 2 for our case. An equivalent result is found for any pair of $E_{DiAj}^{diab}(d_L, d_R)$ and $E_{AjDi}^{diab}(d_L, d_R)$ excited state surfaces, so that the following discussion also holds for them. The diabatic energy surfaces correspond to the (CeCl₆)³⁻-(CeCl₆)²⁻ pair (red surface) and to the (CeCl₆)²⁻-(CeCl₆)³⁻ pair (blue surface), respectively. Their respective minima are found where the left and right distances d_L and d_R take the values of the donor (CeCl₆)³⁻ and acceptor (CeCl₆)²⁻ ground state Ce-Cl equilibrium distances, d_{eD} and d_{eA} (2.660 Å and 2.542 Å in our case; see below), and viceversa: (d_{eD}, d_{eA}) and (d_{eA}, d_{eD}). The energies at the minima are equal: $E_{D0A0}^{diab}(d_{eD}, d_{eA}) = E_{A0D0}^{diab}(d_{eA}, d_{eD}) = E_{e,D0A0}$.

The DA and AD diabatic surfaces are degenerate along the $d_L=d_R$ line. So, the diabatic activated complex of the $D+A \rightarrow A+D$ electron transfer reaction, which is the crossing point between the two surfaces with lowest energy, can be found by minimization of any of the two surfaces along the $d_L=d_R$ line. (Strictly speaking, the activated complex is the full $d_L=d_R$ line, but here we will use the term only for its most stable structure.) In the diabatic activated complex, which is expected to be close to the adiabatic, the left and right distances take a common value d_{ac} . In our case, the minimum is found at a common Ce-Cl distance of the donor (CeCl₆)³⁻ and the acceptor (CeCl₆)²⁻ of $d_{ac}=2.599$ Å.

A fairly good estimation of d_{ac} can be obtained from the

harmonic approximation of the diabatic surfaces. In this approximation, the activated complex is found at $d_{ac} = (\omega_D^2 d_{eD} + \omega_A^2 d_{eA}) / (\omega_D^2 + \omega_A^2)$, ω_D and ω_A being the vibrational frequencies of D and A ground states respectively. In other words, d_{ac} would be the ω^2 -weighted average of donor and acceptor equilibrium distances. If equal values for the vibrational frequencies of donor and acceptor are assumed, as it is done in the vibronic model of Piepho *et al.*,⁹ d_{ac} is the simple average, $d_{ac} = (d_{eD} + d_{eA})/2$. Since the acceptor has a higher force constant than the donor, d_{ac} should be close to the average of d_{eD} and d_{eA} but closer to d_{eA} than to d_{eD} . The values $\omega_D=313 \text{ cm}^{-1}$ and $\omega_A=355 \text{ cm}^{-1}$ found in the present *ab initio* calculations (see below) give $d_{ac}=2.594 \text{ \AA}$ for the different-frequencies harmonic approximation and $d_{ac}=2.601 \text{ \AA}$ for the equal-frequencies harmonic approximation. Both of them are close to the found $d_{ac}=2.599 \text{ \AA}$, although, interestingly, the latter is closer. It is a manifestation of the fact that anharmonicity increases the Ce-Cl distance of the activated complex, as it does with the equilibrium distances of donor and acceptor. It means that there is a compensation of the errors due to assuming equal force constants and neglect-

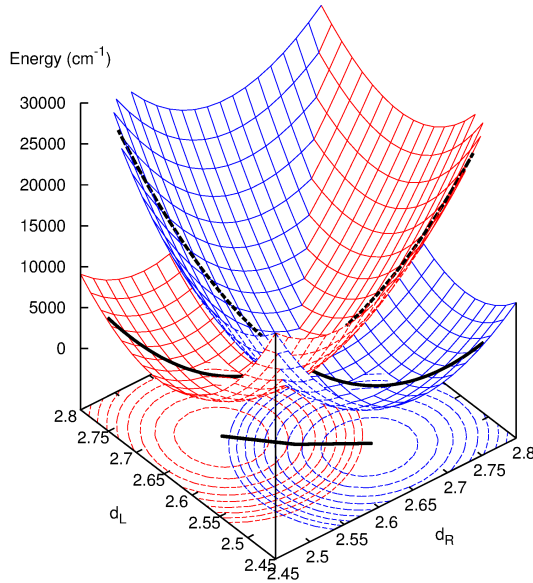


FIG. 2: Diabatic potential energy surfaces of the DA mixed valence pair $(\text{CeCl}_6)^{3-}-(\text{CeCl}_6)^{2-}$ (red) and the AD mixed valence pair $(\text{CeCl}_6)^{2-}-(\text{CeCl}_6)^{3-}$ (blue) in their ground states. d_L and d_R stand for the Ce-Cl distances in the left and right clusters, respectively. Black straight lines on the d_L - d_R plane connect the position of activated complex of the electron transfer reaction with the equilibrium positions of the pairs; these straight lines define the electron transfer reaction coordinate. The lowest (full lines) and highest (dashed lines) diabatic energies along the reaction coordinate are shown on the surfaces.

ing anharmonicity.

The diabatic electron transfer activation energy is $E_{DOA0}^{\ddagger \text{diab}} = E_{DOA0}^{\text{diab}}(d_{ac}, d_{ac}) - E_{e,DOA0}$. It is independent of the d_{DA} distance between donor and acceptor (within approximation 2 of Sec. II B 2) and it is an upper bound of the adiabatic activation energy, which is d_{DA} -dependent.

The ground state diabatic electron transfer reaction coordinate Q_{et} can be approximated with the straight lines that connect the activated complex (d_{ac}, d_{ac}) with the two minima (d_{eD}, d_{eA}) and (d_{eA}, d_{eD}) . This reaction coordinate is represented in Fig. 2 in the d_L - d_R plane. The DA pair has the lowest diabatic energy in the left side of the activated complex ($d_L > d_R$) and the AD pair in the right side ($d_L < d_R$), in correspondance with the larger size of D at equilibrium. The lowest and highest diabatic energies along the reaction coordinate are shown in Fig. 2 with full and dashed lines, respectively, drawn on the surfaces. Since these lines contain the most interesting information of the diabatic energy surfaces, it is convenient to plot them in energy diagrams along the reaction coordinate (as the dashed lines in Fig. 1) instead of the more cumbersome energy surfaces, i.e. E vs. Q_{et} instead of E vs. (d_L, d_R) .

For a precise definition of Q_{et} , we can recall that the changes of the Ce-Cl distances in the left and right clusters d_L and d_R along the reaction coordinate fulfil

$$d_L - d_{ac} = m(d_R - d_{ac}) \begin{cases} m = \frac{d_{eD} - d_{ac}}{d_{eA} - d_{ac}} : d_L \geq d_R \\ m = \frac{d_{eA} - d_{ac}}{d_{eD} - d_{ac}} : d_L \leq d_R \end{cases} . \quad (7)$$

Then, the normal reaction coordinate can be written as

$$Q_{et} = \frac{1}{\sqrt{1+m^2}} (Q_R + mQ_L) , \quad (8)$$

Q_L and Q_R being the normal breathing modes of the left and right CeCl_6 moieties with respect to their structures in the activated complex:

$$Q_L = \frac{1}{\sqrt{6}} (\delta_{Cl_{L1}} + \delta_{Cl_{L2}} + \dots + \delta_{Cl_{L6}}) ,$$

$$Q_R = \frac{1}{\sqrt{6}} (\delta_{Cl_{R1}} + \delta_{Cl_{R2}} + \dots + \delta_{Cl_{R6}}) , \quad (9)$$

which have been expressed in terms of the displacements $\delta_{Cl_{Lk}}$ and $\delta_{Cl_{Rk}}$ of the chlorine atoms in the left and right CeCl_6 moieties away from their respective Ce atoms, starting from the positions they occupy in the activated complex. A graphical representation of the Cl displacements along Q_{et} is shown in Fig. 3. Since the left and right cluster breathings imply $\delta_{Cl_{L1}} = \delta_{Cl_{L2}} = \dots = d_L - d_{ac}$ and $\delta_{Cl_{R1}} = \delta_{Cl_{R2}} = \dots = d_R - d_{ac}$, we can write

$$Q_L = \sqrt{6}(d_L - d_{ac}) ,$$

$$Q_R = \sqrt{6}(d_R - d_{ac}) , \quad (10)$$

and

$$Q_{et} = \sqrt{6/(1+m^2)} [(d_R - d_{ac}) + m(d_L - d_{ac})]$$

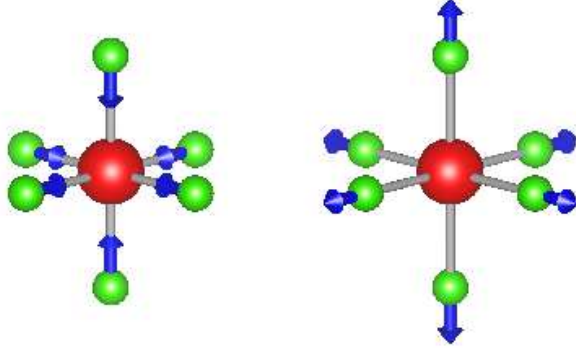


FIG. 3: Displacements of the Cl atoms of the $\text{CeCl}_6\text{-CeCl}_6$ moieties along the electron transfer reaction coordinate Q_{et} .

$$\begin{aligned}
 &= \sqrt{6(1+m^2)}(d_R - d_{ac}) \\
 &= \sqrt{6(1+m^2)}(d_L - d_{ac})/m.
 \end{aligned} \tag{11}$$

We may mention the relationship between this reaction coordinate and the one of the vibronic model of Piepho *et al.*⁹ The latter corresponds to $d_{ac} = (d_{eD} + d_{eA})/2$, which implies $m = -1$ and gives $Q_{et} = (Q_R - Q_L)/\sqrt{2} = \sqrt{3}(d_R - d_L)$. We observed that this is a rather good approximation in our case.

III. DETAILS OF THE QUANTUM MECHANICAL CALCULATIONS

In this Section we describe the details of the quantum mechanical calculations of the $E_{D_i}(d_{\text{Ce-Cl}})$ and $E_{A_j}(d_{\text{Ce-Cl}})$ components of the mixed valence pair energies in Eq. 6. As donor D and acceptor A we adopted, respectively, the $(\text{CeCl}_6\text{Li}_6\text{Cs}_8)^{11+}$ and $(\text{CeCl}_6\text{Li}_6\text{Cs}_8)^{12+}$ clusters. We performed *ab initio* wave function theory embedded cluster quantum chemical calculations on these clusters embedded in the $\text{Cs}_2\text{LiLuCl}_6$ elpasolite host with the MOLCAS suite of programs.²¹ The calculations include bonding interactions, static and dynamic electron correlation effects, and scalar and spin-orbit coupling relativistic effects within the clusters, which are treated at a high theoretical level. They also include Coulomb, exchange, and Pauli repulsion interactions between the host and the clusters, which are considered at a lower theoretical level by means of a quantum mechanical embedding potential. Electron correlation effects between the cluster and the host are excluded from these calculations.

The embedded cluster calculations are two-step spin-orbit coupling SA-CASSCF/MS-CASPT2/RASSI-SO DKH calculations. In the first step, we used the many-electron scalar relativistic second-order Douglas-Kroll-Hess (DKH) Hamiltonian.^{22,23} In $\text{Cs}_2\text{LiLuCl}_6:(\text{CeCl}_6\text{Li}_6\text{Cs}_8)^{11+}$,

we performed state-average complete-active-space self-consistent-field²⁴⁻²⁶ (SA-CASSCF) calculations with the active space that results from distributing one active electrons in 13 active molecular orbitals with main character Ce 4*f*, 5*d*, and 6*s*. The equivalent calculation in $\text{Cs}_2\text{LiLuCl}_6:(\text{CeCl}_6\text{Li}_6\text{Cs}_8)^{12+}$ is a closed-shell Hartree-Fock SCF calculation. These calculations provided occupied and empty molecular orbitals to feed subsequent multi-state second-order perturbation theory calculations (MS-CASPT2),²⁷⁻³⁰ where the dynamic correlation of the Ce 5*s*, 5*p*, Cl 3*s*, 3*p*, and Cs 5*p* electrons was taken into account. We used the standard IPEA value (0.25 au).³¹

In the second step, we included spin-orbit coupling effects by adding the Atomic Mean Field Integrals approximation (AMFI) of the DKH spin-orbit coupling operator³² to the scalar relativistic Hamiltonian. In this step, we used the spin-free-state-shifting operator as a means to combine spin-orbit couplings calculated with statically correlated wave functions and spin-orbit free energies calculated with dynamic correlation³³ and, accordingly, we performed restricted-active-space state-interaction spin-orbit calculations (RASSI-SO)^{34,35} with the transformed CASSCF wave functions (first-order wave functions of the MS-CASPT2 method) and the MS-CASPT2 energies.

We considered O_h nuclear configurations of the clusters with varying Ce-Cl distance. The calculations were performed using the abelian D_{2h} symmetry group. The spin-orbit coupling states of the donor $(\text{CeCl}_6\text{Li}_6\text{Cs}_8)^{11+}$ are the following Kramers doublets: For the *ungerade* 4*f*¹ configuration, one double degenerate Γ_{6u} of ${}^2T_{1u}$ character, two double degenerate Γ_{7u} of ${}^2A_{2u}$ and ${}^2T_{2u}$ characters, and two quadruple degenerate Γ_{8u} of ${}^2T_{1u}$ and ${}^2T_{2u}$ characters; for the *gerade* 5*d*¹ and 6*s*¹ configurations, one double degenerate Γ_{6g} of ${}^2A_{1g}$ character, one double degenerate Γ_{7g} of ${}^2T_{2g}$ characters, and two quadruple degenerate Γ_{8g} of ${}^2T_{2g}$ and 2E_g characters. The closed-shell acceptor $(\text{CeCl}_6\text{Li}_6\text{Cs}_8)^{12+}$ has one A_{1g} state of ${}^1A_{1g}$ character.

We used the following gaussian basis set: All-electron atomic natural orbital (ANO) relativistic basis sets for cerium,³⁶ chlorine,³⁷ and lithium,³⁸ with respective contractions (25s22p15d11f4g2h)/[9s8p5d4f3g2h], (17s12p5d4f)/[5s4p2d1f], and (14s9p)/[4s3p]. For cesium, we used a [Cd]-core *ab initio* model potential (AIMP)³⁹ that was obtained in this work from the 1s-5s, 2p-4p, 3d-4d relativistic core ANOs of Ref. 38, and a valence basis set from the same reference with the contraction (26s22p15d)/[6s5p2d].

The Hamiltonian of the $(\text{CeCl}_6\text{Li}_6\text{Cs}_8)^{11+}$ and $(\text{CeCl}_6\text{Li}_6\text{Cs}_8)^{12+}$ clusters was supplemented with the AIMP embedding potential⁴⁰ of $\text{Cs}_2\text{LiLuCl}_6$, which has been obtained in this work. This embedding potential is made of: 1) total-ion embedding AIMPs representing Cs^+ , Li^+ , and Lu^{3+} cations and Cl^- anions, which are located at experimental sites of the $\text{Cs}_2\text{LiLuCl}_6$ lattice, within a cube made of $2 \times 2 \times 2$ unit cells and centered on Lu^{3+} , and 2) a set of 25271 additional point charges situated at lattice sites, generated by the zero-multipole method of Gellé and Lepetit,⁴¹ which closely reproduce the Ewald potential⁴²

within the clusters. The experimental crystal structure of $\text{Cs}_2\text{LiLuCl}_6$ (Ref. 43) is the following: Space group number 225, Fm3m cubic; lattice constant $a=10.409$ Å, $x(\text{Cl})=0.2483$. The embedding AIMPs have been obtained in self-consistent embedded-ions (SCEI)⁴⁴ Hartree-Fock (HF) calculations.

The [Cd]-core AIMP of Cs and the embedding AIMP of $\text{Cs}_2\text{LiLuCl}_6$ produced in this work are available from the authors⁴⁵ and are included in the supplementary material.

IV. RESULTS AND DISCUSSION

In this Section we discuss the results of the calculations, which we use for a better understanding of the excited states of Ce-doped $\text{Cs}_2\text{LiLuCl}_6$. We ultimately show that

the never reported IVCT luminescence has in fact been observed in this material. For convenience, we summarize first the experimental energies of the excited states in Sec. IVA. We discuss in Sec. IVB the states that are associated with the Ce^{3+} active center and in Sec. IVC those associated with the $\text{Ce}^{3+}\text{-Ce}^{4+}$ active pairs, which are ultimately responsible for the IVCT luminescence.

A. Excited states of Ce-doped $\text{Cs}_2\text{LiLuCl}_6$

The experimental energies of the excited states of Ce-doped $\text{Cs}_2\text{LiLuCl}_6$ after Ref. 14 are summarized in the first four columns of Table I. In the last three columns we summarize the results of this work, which are discussed below in detail.

TABLE I: Excited states of Ce-doped $\text{Cs}_2\text{LiLuCl}_6$ after the experiments from Reference 14 and this work.

Feature	nm	Experiment cm^{-1}	Assignment	Assignment	This work Process	cm^{-1}
Emission spectrum peaks (with $4f \rightarrow 5de_g$ excitation)						
E1	405,372	24700,26900	$5dt_{2g} \rightarrow 4f$ (${}^2F_{7/2}, {}^2F_{5/2}$)	same	2	20200-23300
E2	275 (257-293) ^a	36400 (34100-38900) ^a	anomalous state $\rightarrow 4f$	IVCT $\text{Ce}^{3+}5de_g \rightarrow \text{Ce}^{4+}_{\text{sts}} 4f$	7	32000-35300
Excitation spectrum peaks (monitoring $5dt_{2g} \rightarrow 4f$ emission)						
A1	>330	<30300	$4f \rightarrow 5dt_{2g}$	same	1	24500, 25700
A2 ^b	216.5,210	46190,47600	$4f \rightarrow 5de_g$ (JT split)	same	3	46100 (45300,46900) ^c
A3	303	33000	unassigned	IVCT $\text{Ce}^{3+}4f \rightarrow \text{Ce}^{4+}_{\text{sts}} 5dt_{2g}$	8	31010,32170
A4	280	35700	lower symmetry Ce^{3+}			
A5	264,243	37900,41200	lower symmetry Ce^{3+}			
A6	198	50500	host self-trapped exciton			
A7	182	54900	impurity-trapped exciton	IVCT $\text{Ce}^{3+}4f \rightarrow \text{Ce}^{4+}_{\text{sts}} 5de_g$	6	56240
A8	176	56800	free excitons	$4f \rightarrow a_{1g,ITE}$	5	59190
Excitation spectrum peaks (monitoring the anomalous emission)						
A2	216.5,210	46190,47600	$4f \rightarrow 5de_g$ (JT split)	same	3	46100 (45300,46900) ^c
A9	184	54300		IVCT $\text{Ce}^{3+}4f \rightarrow \text{Ce}^{4+}_{\text{sts}} 5de_g$	6	56240
A10	174	57500		$4f \rightarrow a_{1g,ITE}$	5	59190
Non-observed transitions						
				$5de_g \rightarrow 4f$ emission	4	43000-46030
				IVCT emission $\text{Ce}^{3+}5dt_{2g} \rightarrow \text{Ce}^{4+}_{\text{sts}} 4f$		13500-16800
				IVCT absorption $\text{Ce}^{3+}4f \rightarrow \text{Ce}^{4+}_{\text{sts}} 4f$	9	10000-13300

^aFull width at half maximum at 290 K.

^bAbsent at low temperature.

^cA 1600 cm^{-1} splitting between the two peaks of the Jahn-Teller split absorption is calculated at room temperature out of $\Delta E_{\text{peaks}} = 2\sqrt{2E_{JT}kT}$ (Reference 46).

The manifold of excited states is made of: states associated with the $4f^1$, $5dt_{2g}^1$, and $5de_g^1$ configurations of Ce^{3+} , an

impurity-trapped exciton (ITE) also associated with Ce^{3+} ,

and self-trapped exciton and free exciton host states. Besides them, an anomalous state has been found necessary to explain an anomalous emission.¹⁴ Interesting features of the anomalous emission are: it is excited by $4f \rightarrow 5de_g$ absorptions but not by excitations to the host conduction band, its energy is much lower than its excitation (large Stokes shift) and higher than the $4f \rightarrow 5dt_{2g}$ absorptions, it is a much wider band than the regular $\text{Ce}^{3+} 5d \rightarrow 4f$ emissions, and its intensity increases with temperature up to 250 K and decreases above this. In order to understand these properties, the existence of an anomalous state that emits to the $4f$ ground state was suggested.¹⁴ This state would have an energy intermediate between the $5dt_{2g}$ and $5de_g$ manifolds and it would be populated after an auto-ionization of the electron from $5de_g$ to the conduction band such that it would remain near Ce. The true nature of the anomalous state remained not fully clear.¹⁴

B. Ce^{3+} active center

The energy levels of the $(\text{CeCl}_6\text{Li}_6\text{Cs}_8)^{11+}$ cluster embedded in $\text{Cs}_2\text{LiLuCl}_6$ resulting from the spin-orbit coupling *ab initio* calculation are represented in Fig. 4 as a function of the Ce-Cl distance $d_{\text{Ce-Cl}}$ along the a_{1g} breathing mode of the CeCl_6 moiety. We include in the Figure the total energy of the $(\text{CeCl}_6\text{Li}_6\text{Cs}_8)^{12+}$ embedded cluster in the same energy scale. This means that the energy difference between the $A_{1g}({}^1A_{1g})$ ground state of Ce^{4+} center (dashed red line) and the $1\Gamma_{7u}({}^2A_{2u})$ state of Ce^{3+} center (lowest full black line) corresponds to the ionization potential of Ce^{3+} , not to the conduction band of the host, but to the vacuum. Equilibrium Ce-Cl bond lengths and breathing mode vibrational frequencies of all states, adiabatic transition energies (minimum-to-minimum), and vertical (or Frank-Condon) transition energies calculated at significant values of $d_{\text{Ce-Cl}}$, are given in Table II.

The calculations give standard $4f^1$ and $5d^1$ manifolds, like in $\text{Cs}_2\text{NaYCl}_6:\text{Ce}^{3+}$ (Ref. 47), and a high energy impurity-trapped exciton state, like those previously found in $\text{Cs}_2\text{GeF}_6:\text{U}^{4+}$ (Ref. 48) and $\text{SrCl}_2:\text{Yb}^{2+}$ (Ref. 49). They support the assignments of the so called normal features of the excitation and emission spectra made in Ref. 14.

The $4f \rightarrow 5dt_{2g}$ absorption and $5dt_{2g} \rightarrow 4f$ emission (1 and 2 in Fig. 4 and Table II) are calculated at 24500-25700 cm^{-1} and 20200-23350 cm^{-1} respectively. The emission is split in two bands, one with three components peaking at 20200-21000 cm^{-1} due to the crystal-field splitting of $4f^{1-2}F_{7/2}$, and another with two components peaking at 22750-23350 cm^{-1} due to the crystal-field splitting of $4f^{1-2}F_{5/2}$. In Fig. 5a we show the simulation of the shape of these absorption (blue lines) and emission (green lines) bands. They have been calculated using the semiclassical time-dependent approach of Heller⁵⁰⁻⁵² assuming harmonic vibrations on the initial and final electronic states. We used a common vibrational frequency of 316 cm^{-1} and the oscillator strengths computed at the respective equilibrium geometries of the ground state (absorption)

and the respective excited states (emissions), which are shown in Table IV of Additional Material. Experimentally, $4f \rightarrow 5dt_{2g}$ was found below 30300 cm^{-1} in the excitation spectrum (its maximum was not reported) and $5dt_{2g} \rightarrow 4f$ split in two bands peaking at 24700 and 26900 cm^{-1} in the emission spectrum (A1 and E1 in Table I).

The $4f \rightarrow 5de_g$ absorption (3 in Fig. 4 and Table II) is calculated as centered at 46100 cm^{-1} , split by an $E \otimes e_g$ Jahn-Teller coupling with Jahn-Teller energy $E_{JT}=1670$ cm^{-1} . In the excitation spectrum, this transition was found as a Jahn-Teller split band with peaks at 46190 and 47600 cm^{-1} (A2 in Table I). The position of the band is well reproduced and its splitting corresponds to a Jahn-Teller energy not far from the calculated one. The $5de_g \rightarrow 4f$ emission (4 in Fig. 4 and Table II) is calculated split in two bands: one with peaks at 43000-43700 cm^{-1} and another with peaks at 45500-46000 cm^{-1} . In Fig. 5b we show the simulation of the shape of these absorption (blue lines) and emission (green lines) bands, without considering the effects of the Jahn-Teller coupling and using the oscillator strengths of Table IV of Additional Material. This emission was not found experimentally, which was interpreted as due to non-radiative decay to an anomalous state.¹⁴ The lack of this emission in Ce-doped $\text{Cs}_2\text{LiYCl}_6$ was interpreted in the same way¹⁶; in Ce-doped $\text{Cs}_2\text{NaYCl}_6$

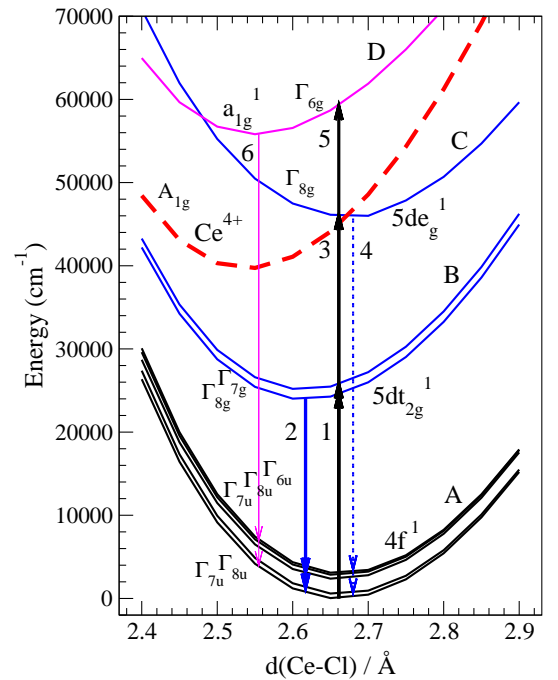


FIG. 4: Energy diagram of the Ce^{3+} active center: Total energies of the states of the $(\text{CeCl}_6\text{Li}_6\text{Cs}_8)^{11+}$ cluster embedded in $\text{Cs}_2\text{LiLuCl}_6$ vs. the Ce-Cl distance along the totally symmetric breathing vibrational mode. Spin-orbit coupling RASSI calculations. Energy scale relative to the ground state energy at equilibrium. The energy of the ground state of the Ce^{4+} center in the same scale, as corresponds to the embedded $(\text{CeCl}_6\text{Li}_6\text{Cs}_8)^{12+}$ cluster, is also shown (dashed red line). See text.

the responsibility of Pr³⁺ and/or Nd³⁺ killer sites, which are present in low concentrations and absorb in the same energy region, was considered instead.⁴⁷ In overall, the calculations of the 5d¹ manifold underestimate the energy of ²T_{2g} and give a good energy of ²E_g; this indicates an overestimation of the crystal-field splitting (10Dq) together

with an underestimation of the 5d¹ barycenter. ²T_{2g} energy underestimations of 2500 cm⁻¹ and ²E_g good energies were previously found in similar calculation on Ce-doped Cs₂NaYCl₆ (Ref. 47).

TABLE II: Spectroscopic constants of the Ce³⁺ and Ce⁴⁺ individual centers in Ce-doped Cs₂LiLuCl₆: Ce-Cl equilibrium distance $d_{\text{Ce-Cl},e}$, breathing mode harmonic vibrational frequency $\omega_{a_{1g}}$ (cm⁻¹), and minimum-to-minimum transition energy T_e . Total energy differences calculated at the equilibrium geometries of the lowest states of the 4f¹, 5dt_{2g}¹, 5de_g¹, and ITE-a_{1g}¹ configurations of Ce³⁺, and of the ground state of Ce⁴⁺. Energies in cm⁻¹, distances in Å. Identification of energy differences with the absorption and emission transitions of Fig. 4 are shown in parentheses.

Branch	State	$d_{\text{Ce-Cl},e}$	$\omega_{a_{1g}}$	T_e	$d_{\text{Ce-Cl}}$ (Å)				
					2.660	2.618	2.669	2.555	2.542
A	Ce ³⁺ 4f ¹					(2)	(4)	(6)	
	1Γ _{7u} (² A _{2u})	2.660	313	0	0	-23340	-46030	-52050	-34880
	1Γ _{8u} (² T _{2u})	2.662	314	530	540	-22740	-45500	-51360	-34160
	2Γ _{7u} (² T _{2u})	2.660	314	2340	2340	-21010	-43690	-49720	-32550
	2Γ _{8u} (² T _{1u})	2.662	314	2800	2800	-20490	-43230	-49120	-31920
	1Γ _{6u} (² T _{1u})	2.663	314	3040	3040	-20220	-43000	-48800	-31590
B	Ce ³⁺ 5dt _{2g} ¹				(1)				
	1Γ _{8g} (² T _{2g})	2.618	318	23930	24500	0	-21290	-30620	-13860
	1Γ _{7g} (² T _{2g})	2.618	319	25120	25710	1190	-20080	-29460	-12710
C	Ce ³⁺ 5de _g ¹				(3)				
	2Γ _{8g} (² E _g) ^a	2.669	322	45860	46070	22910	0	-5780	11370
D	Ce ³⁺ ITE-a _{1g} ¹				(5)				
	1Γ _{6g} (² A _{1g})	2.555	325	55810	59190	33220	13690	0	16170
	Ce ⁴⁺ + e ⁻ (vacuum)								
	A _{1g} (¹ A _{1g})	2.542	355	39690	44870	18050	-420	-16050	0

^aThe calculation of the $E \otimes e_g$ Jahn-Teller coupling of the 2Γ_{8g}(²E_g) state gives a D_{4h} equilibrium structure with the following data: $\delta_{e_g} = 0.081$ Å, $d_{\text{Ce-Cl},\text{ax}} = 2.831$ Å, $d_{\text{Ce-Cl},\text{eq}} = 2.588$ Å, $\omega_{e_g} = 228$ cm⁻¹, $E_{JT} = 1670$ cm⁻¹, $T_e(\Gamma_{6g}(\supset A_{1g})) = 44190$ cm⁻¹, and an energy barrier between equivalent minima of 1200 cm⁻¹: $T_e(\Gamma_{7g}(\supset B_{1g})) = 45390$ cm⁻¹.

A weak broad band in the excitation spectra peaking at 182 nm (54900 cm⁻¹) was assigned to an impurity-trapped exciton and next to it, at 176 nm (56800 cm⁻¹), another more intense but still weak broad band was assigned to free excitons¹⁴ (A7 and A8 in Table I). The calculations give a Γ_{6g} state of ITE-a_{1g}¹ character 55800 cm⁻¹ above the ground state, with the maximum of the absorption band at 59200 cm⁻¹ (5 in Fig. 4 and Table II). This state has an equilibrium Ce-Cl distance of 2.555 Å, which is much shorter than in the 4f¹, 5dt_{2g}¹ and 5de_g¹ states and not far from the 2.542 Å of the Ce⁴⁺ center. Its vibrational frequency (325 cm⁻¹) is only slightly larger than in the 4f¹, 5dt_{2g}¹ and 5de_g¹ states and it does not get as close to the 355 cm⁻¹ of the Ce⁴⁺ center. Its emission is predicted at 48800-52050 cm⁻¹ (6 in Fig. 4 and Table II). In Fig. 5c

we show the simulation of the shape of these absorption (blue lines) and emission (green lines) bands. The oscillator strengths of Table IV of Additional Material have been used for the emission band. The absorption is electric dipole forbidden in O_h symmetry and we used an arbitrary oscillator strength. In this way we are able to see the band shape, which is made of a very long vibrational progression; note, however, that the intensities of the absorption and emission band in Fig. 5c cannot be compared.

The calculations of the Ce³⁺ center do not give any state that could be considered responsible for the very broad emission at 36400 cm⁻¹. This is so in spite of the fact that the basis sets and spaces used in the calculations are flexible enough to reveal the existence electron-hole electronic structures, like those associated so far with the excited states responsible for anomalous luminescence in

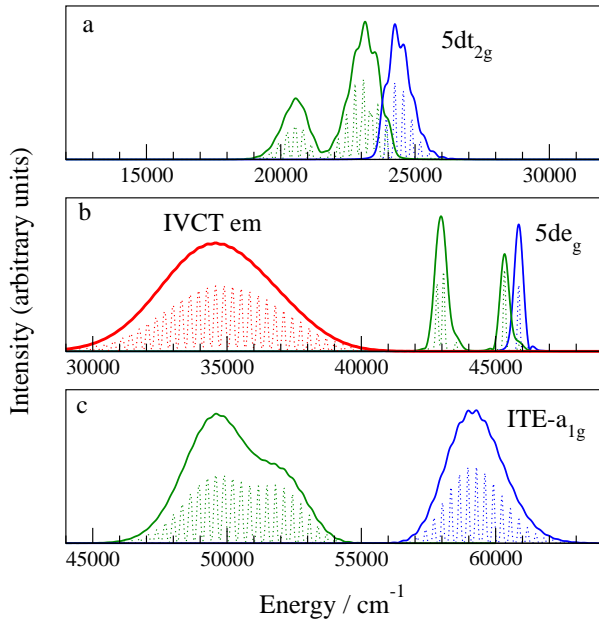


FIG. 5: Simulated absorption and emission band shapes.

lanthanide-doped crystals, should they occur.^{53–55}

C. Ce^{3+} – Ce^{4+} active pair

It is not uncommon that Ce^{4+} is present in Ce^{3+} -doped solids.¹² Having in mind the possibility that this is the case in Ce^{3+} -doped elpasolites, we discuss in this Section the basics of the electronic structure of the Ce^{3+} – Ce^{4+} pairs in Ce -doped $\text{Cs}_2\text{LiLuCl}_6$. We show what absorptions and emissions can take place that are associated with these pairs and cannot be present in single Ce^{3+} active centers. In particular, we focus on the intervalence charge transfer luminescence that can be responsible for the so called anomalous luminescence of this material.

The diabatic potential energy surfaces of the ground and excited states of the Ce^{3+} – Ce^{4+} active pair as functions of the Ce-Cl distances in the left and right CeCl_6 moieties have been calculated using Eq. 6 as described in Sec. II B. Those of the ground state are shown in Fig. 2. Their main features are summarized in Table III. The energies of the states as functions of the ground state electron transfer reaction coordinate are shown in Fig. 6. In Fig. 7 of Additional Material we represent them as functions of the electron transfer reaction coordinates of excited states. Let us briefly describe the meaning of the notation in these Figures and in Table III.

The A branch contains the $[4f^1, A_{1g}]$ electronic states of the Ce^{3+} – Ce^{4+} pair. The A_{et} branch contains the states of the Ce^{4+} – Ce^{3+} pair that result from the A branch after electron transfer from Ce^{3+} to Ce^{4+} . The thermal conversion of the A states into A_{et} states are the electron transfer reactions

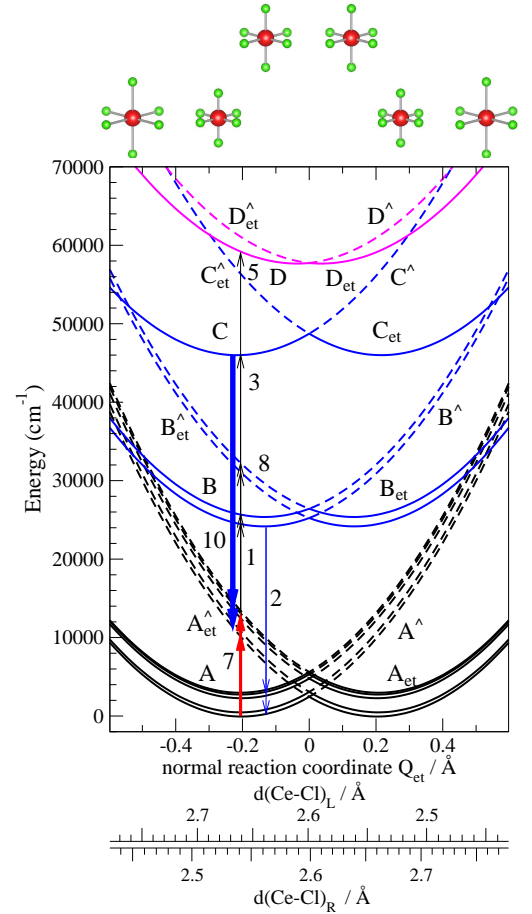
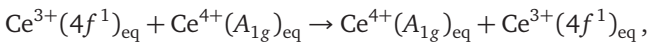
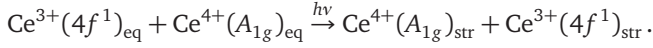


FIG. 6: Diabatic IVCT energy diagram for Ce^{3+} – Ce^{4+} embedded pairs: Total energies of the $(\text{CeCl}_6)^{3-}$ – $(\text{CeCl}_6)^{2-}$ cluster pair embedded in $\text{Cs}_2\text{LiLuCl}_6$ vs. the electron transfer reaction coordinate of the ground state. Ce-Cl distances of the left and right CeCl_6 moieties, $d(\text{Ce}-\text{Cl})_L$ and $d(\text{Ce}-\text{Cl})_R$, are indicated in the lower scale; both of them are equal to 2.599 Å in the activated complex. A qualitative representation of the moieties in the left and right branches and in the activated complex is shown at the top. Energy scale relative to the ground state energy at equilibrium. See text for a description of the labels.

which involve energy barriers. The diabatic barriers shown in Fig. 6 are upper bounds of the adiabatic barriers that result after consideration of the electronic couplings. The A^\wedge branch represents the stressed A states, i.e. the $[4f^1, A_{1g}]$ states of the Ce^{3+} – Ce^{4+} pair with structures close to the equilibrium structure of the Ce^{4+} – Ce^{3+} pair in $[A_{1g}, 4f^1]$ states. Equivalently, the A_{et}^\wedge branch represents stressed states after electron transfer from the A branch, i.e. the $[A_{1g}, 4f^1]$ states of the Ce^{4+} – Ce^{3+} pair with structures close to the equilibrium structure of the $[4f^1, A_{1g}]$ states of the Ce^{3+} – Ce^{4+} pair. Going from branch A^\wedge to A is the non-radiative decay of the $[4f^1, A_{1g}]$ states to their equilibrium structure, which involves the release of the reorganization energy. Obviously, this is energetically equivalent to the non-radiative decay of the $[A_{1g}, 4f^1]$ states, i.e. going from

branch A_{et}^{\wedge} to A_{et} . The vertical transitions from branch A to A_{et}^{\wedge} are the intervalence charge transfer absorptions, which take place with fixed nuclei positions (7 in Fig. 6 and Table III)



They would immediately be followed by the non-radiative decay to A_{et} , which involves the simultaneous relaxation of the coordination shells of Ce^{4+} and Ce^{3+} ,

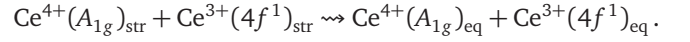


TABLE III: Absorption and emission peak positions of the Ce^{3+} - Ce^{4+} pair in Cs₂LiLuCl₆, calculated as total energy differences at the equilibrium geometries of the lowest states of the $4f^1$, $5dt_{2g}^1$, $5de_g^1$, and ITE- a_{1g}^1 configurations of Ce^{3+} and of the A_{1g} state of Ce^{4+} . $d_{\text{Ce-Cl,L}}$, $d_{\text{Ce-Cl,R}}$ and $d_{\text{Ce-Cl,AC}}$ are the Ce-Cl distances in the left and right CeCl₆ moieties and in the activated complex, respectively. Energies in cm⁻¹, distances in Å. Identification of energy differences with absorption and emission transitions of Fig 6 are shown in parentheses.

		Absorption and emission peaks			
$d_{\text{Ce-Cl,L}}, d_{\text{Ce-Cl,R}}$:		2.660,2.542	2.618,2.542	2.669,2.542	2.555,2.542
Initial state [$\text{Ce}^{3+}, \text{Ce}^{4+}$]:		4f absorption	$5dt_{2g}$ emission	$5de_g$ emission	a_{1g} ITE emission
Final state		$[1\Gamma_{7u}(^2A_{2u}), A_{1g}] \rightarrow$	$[1\Gamma_{8g}(^2T_{2g}), A_{1g}] \rightarrow$	$[2\Gamma_{8g}(^2E_g), A_{1g}] \rightarrow$	$[1\Gamma_{6g}(^2A_{1g}), A_{1g}] \rightarrow$
Branch					
A	$[\text{Ce}^{3+}(4f^1), \text{Ce}^{4+}]$	$\text{Ce}^{3+} 4f \rightarrow 4f$	$\text{Ce}^{3+} 5dt_{2g} \rightarrow 4f$	$\text{Ce}^{3+} 5de_g \rightarrow 4f$	$\text{Ce}^{3+} \text{ITE-}a_{1g} \rightarrow 4f$
	$\rightarrow [1\Gamma_{7u}(^2A_{2u}), A_{1g}]$	0	23340	46030	52050
	$\rightarrow [1\Gamma_{8u}(^2T_{2u}), A_{1g}]$	540	22740	45500	51360
	$\rightarrow [2\Gamma_{7u}(^2T_{2u}), A_{1g}]$	2340	21010	43690	49720
	$\rightarrow [2\Gamma_{8u}(^2T_{1u}), A_{1g}]$	2800	20490	43230	49120
	$\rightarrow [1\Gamma_{6u}(^2T_{1u}), A_{1g}]$	3040	20220	43000	48800
		(7)	(2)	(4)	(6)
A_{et}^{\wedge}	$[\text{Ce}^{4+}, \text{Ce}^{3+}(4f^1)]_{\text{sts}}$	$\text{Ce}^{3+} 4f \rightarrow \text{Ce}^{4+} 4f$	$\text{Ce}^{3+} 5dt_{2g} \rightarrow \text{Ce}^{4+} 4f$	$\text{Ce}^{3+} 5de_g \rightarrow \text{Ce}^{4+} 4f$	$\text{Ce}^{3+} \text{ITE-}a_{1g} \rightarrow \text{Ce}^{4+} 4f$
	$\rightarrow [A_{1g}, 1\Gamma_{7u}(^2A_{2u})]$	10000	16820	35290	50920
	$\rightarrow [A_{1g}, 1\Gamma_{8u}(^2T_{2u})]$	10720	16100	34570	50200
	$\rightarrow [A_{1g}, 2\Gamma_{7u}(^2T_{2u})]$	12330	14490	32960	48590
	$\rightarrow [A_{1g}, 2\Gamma_{8u}(^2T_{1u})]$	12950	13870	32340	47970
	$\rightarrow [A_{1g}, 1\Gamma_{6u}(^2T_{1u})]$	13290	13530	32000	47630
		(1)	(3)	(10)	(11)
B	$[\text{Ce}^{3+}(5dt_{2g}^1), \text{Ce}^{4+}]$	$\text{Ce}^{3+} 4f \rightarrow 5dt_{2g}$	0	21290	30620
	$\rightarrow [1\Gamma_{8g}(^2T_{2g}), A_{1g}]$	24500		20080	29460
	$\rightarrow [1\Gamma_{7g}(^2T_{2g}), A_{1g}]$	25710			
	(8)				
B_{et}^{\wedge}	$[\text{Ce}^{4+}, \text{Ce}^{3+}(5dt_{2g}^1)]_{\text{sts}}$	$\text{Ce}^{3+} 4f \rightarrow \text{Ce}^{4+} 5dt_{2g}$		14280	29910
	$\rightarrow [A_{1g}, 1\Gamma_{8g}(^2T_{2g})]$	31010		13120	28750
	$\rightarrow [A_{1g}, 1\Gamma_{7g}(^2T_{2g})]$	32170			
	(3)				
C	$[\text{Ce}^{3+}(5de_g^1), \text{Ce}^{4+}]$	$\text{Ce}^{3+} 4f \rightarrow 5de_g$		0	5780
	$\rightarrow [2\Gamma_{8g}(^2E_g), A_{1g}]$	46070			
	(9)				
C_{et}^{\wedge}	$[\text{Ce}^{4+}, \text{Ce}^{3+}(5de_g^1)]_{\text{sts}}$	$\text{Ce}^{3+} 4f \rightarrow \text{Ce}^{4+} 5de_g$			4680
	$\rightarrow [A_{1g}, 2\Gamma_{8g}(^2E_g)]$	56240			
	(5)				
D	$[\text{Ce}^{3+}(\text{ITE-}a_{1g}^1), \text{Ce}^{4+}]$	$\text{Ce}^{3+} 4f \rightarrow \text{ITE-}a_{1g}$			0
	$\rightarrow [1\Gamma_{6g}(^2A_{1g}), A_{1g}]$	59190			
D_{et}^{\wedge}	$[\text{Ce}^{4+}, \text{Ce}^{3+}(\text{ITE-}a_{1g}^1)]_{\text{sts}}$				
	$\rightarrow [A_{1g}, 1\Gamma_{6g}(^2A_{1g})]$	61050			
Branch crossings					
Branch pair and energy barrier		A- A_{et} 2600	B- B_{et} 1100	C- C_{et} 2900	D- D_{et} 50
$d_{\text{Ce-Cl,AC}}$		2.599	2.578	2.600	2.548
Branch pair and energy barrier		B- A_{et}^{\wedge} 5800	C- B_{et}^{\wedge} 5100	D- C_{et}^{\wedge} 1100	
$d_{\text{Ce-Cl,L}}, d_{\text{Ce-Cl,R}}$		2.70, 2.45	2.79, 2.49	2.56, 2.49	

The B , C , and D related branches are equivalent to the A ones, but referred to the states of Ce³⁺ of the $5dt_{2g}^1$ configuration, the $5de_g^1$ configuration, and the ITE- a_{1g}^1 impurity trapped excitonic character, respectively.

In Fig. 6 and Table III we have indicated the photo-processes that take place in the Ce³⁺ active center and are responsible for observed spectroscopic features, as discussed in the previous section: The $4f \rightarrow 5dt_{2g}$, $4f \rightarrow 5de_g$, and $4f \rightarrow \text{ITE-}a_{1g}$ absorptions (**1**, **3**, **5**), and the $5dt_{2g} \rightarrow 4f$ emission (**2**).

1. IVCT absorptions

More interesting now are the photo-processes that involve intervalence charge transfer between Ce³⁺ and Ce⁴⁺. In Fig. 6 they correspond to vertical lines starting in the minimum of one branch (A , A_{et} , B , B_{et} , C , C_{et} , D , D_{et}), drawn with full lines, and ending in one of the stressed branches (A^\wedge , A_{et}^\wedge , B^\wedge , B_{et}^\wedge , C^\wedge , C_{et}^\wedge , D , D_{et}^\wedge), drawn with dashed lines. We have indicated three of them in Fig. 6. All of these transitions give very broad bands because of the large offsets between the minima of their corresponding energy surfaces: A and A_{et} , A and B_{et} , etc. These offsets are given by $\Delta Q = Q_{e,f} - Q_{e,i}$, with the equilibrium coordinates of the final and initial state $Q_{e,f}$ and $Q_{e,i}$ given by Eq. 11. The values of these horizontal offsets are given in Table V of Additional Material. They are approximately equal to $\sqrt{3}(\Delta d_R - \Delta d_L)$, Δd_R and Δd_L being the Ce-Cl bond length changes experienced by the Ce⁴⁺ acceptor center (right) and the Ce³⁺ donor center (left) in the IVCT transition, which, in turn, is about $2\sqrt{3}$ times the difference of Ce-Cl equilibrium distances in the Ce³⁺ and Ce⁴⁺ centers.

Absorption **7**, $A \rightarrow A_{et}^\wedge$, or $[\text{Ce}^{3+}(4f^1), \text{Ce}^{4+}]_{\text{eq}} \rightarrow [\text{Ce}^{4+}, \text{Ce}^{3+}(4f^1)]_{\text{sts}}$, is the photoinduced electron transfer commonly found in mixed valence compounds,^{4,6} i.e. the IVCT absorption. It has been reported in Ce³⁺-doped LaPO₄ by Van Schaik *et al.*¹² It corresponds to the vertical one-electron orbital transition $\text{Ce}^{3+}4f \rightarrow \text{Ce}^{4+}4f$ and it is followed by a strong nuclei reorganization around Ce⁴⁺ and Ce³⁺ in which all the IVCT absorption energy is released: $[\text{Ce}^{4+}, \text{Ce}^{3+}(4f^1)]_{\text{sts}} \rightsquigarrow [\text{Ce}^{4+}, \text{Ce}^{3+}(4f^1)]_{\text{eq}}$. The present calculations predict it for the Ce³⁺-Ce⁴⁺ pair in Cs₂LiLuCl₆ as a very broad band peaking at about 10000-13300 cm⁻¹, which can also occur in other chloroelpasolites. The large width of this band is associated with the large offset between the minima of the A and A_{et} energy surfaces, which is here found to be of about 0.41 Å (cf. Table V of Additional Material).

Absorption **8**, $A \rightarrow B_{et}^\wedge$, or $[\text{Ce}^{3+}(4f^1), \text{Ce}^{4+}]_{\text{eq}} \rightarrow [\text{Ce}^{4+}, \text{Ce}^{3+}(5dt_{2g}^1)]_{\text{sts}}$, is an IVCT absorption of higher energy. It corresponds to the vertical one-electron orbital transition $\text{Ce}^{3+}4f \rightarrow \text{Ce}^{4+}5dt_{2g}$. Its energy is above the regular $\text{Ce}^{3+}4f \rightarrow 5dt_{2g}$ absorption (**1**) and the difference between them is the reorganization energy that is released after the absorption. In this case, it is predicted as

a very broad band peaking at 31000-32200 cm⁻¹, which is 6500 cm⁻¹ above $\text{Ce}^{3+}4f \rightarrow 5dt_{2g}$. Since the latter is underestimated in these calculations, we can expect the same degree of underestimation in this IVCT absorption. The experimental peaks in the excitation spectrum at 33000 cm⁻¹ (A3) and 35700 cm⁻¹ (A4), which are very wide and have been unassigned (A3) or assigned to lower symmetry Ce³⁺ sites¹⁴ (A4) can be assigned to this IVCT absorption. Again, the large width of this band is associated with the large offset between the minima of the A and B_{et} energy surfaces, which is here found to be of about 0.34 Å (cf. Table V of Additional Material).

Absorption **9**, $A \rightarrow C_{et}^\wedge$, or $[\text{Ce}^{3+}(4f^1), \text{Ce}^{4+}]_{\text{eq}} \rightarrow [\text{Ce}^{4+}, \text{Ce}^{3+}(5de_g^1)]_{\text{sts}}$, is an IVCT absorption of even higher energy. Analogously to absorption 8, it is the vertical one-electron orbital transition $\text{Ce}^{3+}4f \rightarrow \text{Ce}^{4+}5de_g$ and its energy is above the regular $\text{Ce}^{3+}4f \rightarrow 5de_g$ absorption (**3**) in an amount equal to the reorganization energy. It is predicted as a very broad band peaking at 56240 cm⁻¹, 10200 cm⁻¹ above $\text{Ce}^{3+}4f \rightarrow 5de_g$. Since the latter is calculated to be close to experiment in these calculations, we can expect analogous agreement in this IVCT absorption. The experimental peak in the excitation spectrum at 54900 cm⁻¹ (A7), can be associated with this IVCT absorption. The fact that the intensity of the A7 band in the excitation spectrum of the dt_{2g} emission is comparable to that of the $\text{Ce}^{3+}4f \rightarrow 5de_g$ (A2) band further suggests this assignment.

2. IVCT luminescence

Emission **10**, $C \rightarrow A_{et}^\wedge$, or $[\text{Ce}^{3+}(5de_g^1), \text{Ce}^{4+}]_{\text{eq}} \rightarrow [\text{Ce}^{4+}, \text{Ce}^{3+}(4f^1)]_{\text{sts}}$, is specially interesting because it is an IVCT emission and, to the best of our knowledge, IVCT emissions have never been reported. As we discuss next, this emission corresponds well with the so called anomalous emission (E2).¹⁴ This IVCT luminescence is the vertical one-electron orbital transition $\text{Ce}^{3+}5de_g \rightarrow \text{Ce}^{4+}4f$ and it is followed by a strong nuclei reorganization around Ce⁴⁺ and Ce³⁺. This involves a large Ce-Cl distance shortening around Ce⁴⁺ and a large Ce-Cl distance elongation around Ce³⁺, and it releases an energy which is very similar to the energy of the IVCT absorption 7. The only difference between these energies arises from the fact that the Ce-Cl equilibrium bond length in the Ce³⁺ center is different in its $5de_g^1$ states and $4f^1$ states, but this difference is much smaller than the offset between the minima of the C and A_{et} branches along the electron transfer normal coordinate Q_{eg} , which determines the reorganization energy. The reorganization energy after the IVCT emission is the amount by which this emission is lower than the $\text{Ce}^{3+}4f \rightarrow 5de_g$ absorption, i.e. it is its Stokes shift. In other words, the Stokes shift of this IVCT emission amounts the ground IVCT absorption 7. This is slightly above 10000 cm⁻¹ in the present calculations. The experimental Stokes shift of the anomalous emission, calculated as the difference between the ex-

perimental $4f \rightarrow 5de_g$ absorption maximum (46900 cm^{-1} average of the JT split excitation) and the anomalous emission maximum (36400 cm^{-1}) is 10500 cm^{-1} .

The calculation predicts this IVCT emission band to be a very wide band with peaks in the $32000\text{-}35300 \text{ cm}^{-1}$ region (Table III). Its simulation is shown in red in Fig. 5b. Since the diabatic calculations do not provide oscillator strengths, we have used the oscillator strengths of the regular $5de_g \rightarrow 4f$ emission in Table IV of Additional Material in order to be able to simulate the band shape. Accordingly, the intensities of the IVCT emission band and the $5de_g \rightarrow 4f$ emission band in Fig. 5b cannot be compared, but we must expect that the different shapes of both emission bands are fairly well reproduced. The IVCT emission is a very broad band with a full width at half maximum (FWHM) of about 5000 cm^{-1} . The experimental FWHM at 290 K is 4800 cm^{-1} . So, both the position and shape of this band correspond well with the anomalous emission (E2). Moreover, the following additional supporting argument on the band width can be given: First, we should expect the IVCT emission **10** to have a band shape very similar to that of the regular IVCT absorption **7**, because both of them have very similar normal coordinate offsets. Second, the band width $\Delta\tilde{\nu}_{1/2}$ (in cm^{-1}) and band maximum $\tilde{\nu}_{max}$ (in cm^{-1}) of the latter are related according to $\Delta\tilde{\nu}_{1/2} = (\tilde{\nu}_{max} 7.71 T)^{1/2}$ at temperatures T (in K) high enough so that $\hbar\omega \ll 2kT$, ω being the vibrational frequency,⁷ and using the experimental Stokes shift of the anomalous emission for $\tilde{\nu}_{max}$, $\tilde{\nu}_{max}=10500 \text{ cm}^{-1}$, we get at T=290 K a FWHM of $\Delta\tilde{\nu}_{1/2}=4850 \text{ cm}^{-1}$, which agrees very well with the experimental FWHM of the anomalous emission.

According to the interpretation given in this paper, the anomalous emission is not due to an electron-hole recombination in which the electron is in the conduction band and the hole in the Ce impurity, and there is no anomalous state. Instead, the emission is an electron transfer from a $5de_g$ orbital of a Ce^{3+} center to a $4f$ orbital of a Ce^{4+} center, which takes place with frozen nuclei positions and leaves the newly formed Ce^{4+} and Ce^{3+} centers in their ground electronic states and under strong structural stress. The large relaxation energy released afterwards is basically the large Stokes shift of this emission. This is graphically represented in Fig. 8 of Additional Material. If an electron-hole recombination description is to be used, the electron is in a Ce^{3+} center and the hole in a Ce^{4+} center, but this kind of description is not very adequate because such a recombination of electron and hole would still leave a hole and an electron.

The principal excitation of the anomalous emission is the $\text{Ce}^{3+} 4f \rightarrow 5de_g$ absorption (A2, cf. Figs. 5c and 5d in Ref. 14); this is in agreement with the emission starting in the $5de_g^1$ manifold. Also, two additional broad peaks have been identified in its excitation spectrum at 54300 cm^{-1} (A9) and 57500 cm^{-1} (A10); they can be made of absorptions from the A branch to the C_{et}^\wedge , D, and D_{et}^\wedge branches, i.e. to $\text{Ce}^{3+}4f \rightarrow \text{Ce}^{4+}5de_g$ IVCT absorption and absorptions to the impurity-trapped exciton. We must note that

the electronic couplings, which are missing in the diabatic energy surfaces, will have a stronger effect on the states of these excited branches. This and the lower symmetry driven splittings also missing here, indicate that the states at about $5000\text{-}10000 \text{ cm}^{-1}$ above the $\text{Ce}^{3+} 5de_g^1$ manifold should be a strong mix of the diabatic states of the C_{et}^\wedge , D, and D_{et}^\wedge branches. They can be responsible for the above mentioned peaks, but also for the peaks at 54900 and 56800 cm^{-1} of the excitation spectrum of the $\text{Ce}^{3+} 5dt_{2g} \rightarrow 4f$ emission (A7, A8). The 56800 cm^{-1} peak was assigned to an impurity-trapped exciton in Ref. 14.

Another specific feature of the anomalous emission of Ce-doped $\text{Cs}_2\text{LiLuCl}_6$ is that it is not excited by absorptions to the conduction band (CB), although these absorptions effectively excite the $5dt_{2g} \rightarrow 4f$ emission.¹⁴ Such absorptions mean an ionization of Ce^{3+} to the CB that destroys the $\text{Ce}^{3+}\text{-Ce}^{4+}$ pair, so that for the anomalous emission to happen, the electron must be transferred back from the CB to the $5de_g$ empty orbital of Ce^{4+} . The present calculation does not give information on this; calculations on metal-to-metal charge transfer in Ce-Lu, Ce-Cs, and Ce-Li pairs will be the subject of further study.

Finally, in Ref. 14 it was shown that the decay time of the anomalous emission excited with the $4f \rightarrow 5de_g$ absorption was found to remain constant from 12 K to 240 K, to start dropping at 240 K (cf. Fig. 8 in Ref. 14), and to quench at 370 K. Following its correlation with the $5dt_{2g} \rightarrow 4f$ emission it was also shown that the anomalous emission is quenched by means of energy transfer to the $5dt_{2g}^1$ states of Ce^{3+} . Fitting the parameters of a kinetic model to the experimental data led them to an activation energy of 2900 cm^{-1} . Parallely, the $4f \rightarrow 5de_g$ absorption was found to excite the $5dt_{2g} \rightarrow 4f$ emission, although no connection with the above activation energy was made.

All these observations are consistent with the present interpretation. In effect, the $C\text{-}B_{et}^\wedge$ crossing is responsible for the decay from the state that emits the anomalous luminescence (though it is a $5de_g^1$ state and not an anomalous state) to the $5dt_{2g}^1$ state. Such crossing gives the activation energy of the thermal process $\text{Ce}^{3+}(5de_g^1) + \text{Ce}^{4+} \rightarrow \text{Ce}^{4+} + \text{Ce}^{3+}(5dt_{2g}^1)$. The diabatic result found here is 5100 cm^{-1} . This value is reduced by the Jahn-Teller splitting of the $5de_g^1$ state, it will be further reduced by the inclusion of electronic couplings and, perhaps more importantly, by a lower crystal-field splitting and by a larger offset between the minima of the C and B_{et} branches. We already commented above that the present calculation overestimates the crystal field splitting and underestimations of the nuclear offsets are common in calculations of this type.⁵⁶ And this interpretation also explains that the $4f \rightarrow 5de_g$ absorption excites the $5dt_{2g} \rightarrow 4f$ emission.

Besides, the quenching of the $5dt_{2g} \rightarrow 4f$ emission can be related to the $B\text{-}A_{et}^\wedge$ crossing, i.e. to the thermal process $\text{Ce}^{3+}(5dt_{2g}^1) + \text{Ce}^{4+} \rightarrow \text{Ce}^{4+} + \text{Ce}^{3+}(4f^1)$. This is found to have a diabatic activation energy of 5800 cm^{-1} , higher than that of the $5de_g^1$ decay but not much. With the same

arguments than before, we should expect this barrier to be reduced upon inclusion of the missing contributions, but not more than the other, so that the results indicate that the activation energy is slightly larger for the non-radiative decay of the $5dt_{2g}^1$ states than of the $5de_g^1$ states. Hence a larger quenching temperature of the $5dt_{2g} \rightarrow 4f$ emission compared with the anomalous emission.

Before ending this discussion we may remark that, according to these results, we may expect the existence of an IVCT emission of lower energy corresponding to the vertical one-electron orbital transition $\text{Ce}^{3+}5dt_{2g} \rightarrow \text{Ce}^{4+}4f$, which is to say to the transition $B \rightarrow A_{et}^{\wedge}$, or $[\text{Ce}^{3+}(5dt_{2g}^1), \text{Ce}^{4+}]_{\text{eq}} \rightarrow [\text{Ce}^{4+}, \text{Ce}^{3+}(4f^1)]_{\text{sts}}$. This transition is expected to appear at an energy lower than the $5dt_{2g} \rightarrow 4f$ emission by an amount very similar the first IVCT absorption, 10000 cm^{-1} in our case, i.e. at about $14000\text{-}16000 \text{ cm}^{-1}$.

The new interpretation of the electronic excited states of Ce-doped $\text{Cs}_2\text{LiLuCl}_6$ is summarized in Table I.

V. CONCLUSIONS

In this paper we report for the first time the existence of intervalence charge transfer luminescence. We have shown that the so called anomalous luminescence of Ce-doped $\text{Cs}_2\text{LiLuCl}_6$, which is characterized mainly by a very large Stokes shift and a very large band width, corresponds to an IVCT emission that takes place in $\text{Ce}^{3+}\text{-Ce}^{4+}$ pairs, in particular to the vertical one-electron orbital transition $\text{Ce}^{3+}5de_g \rightarrow \text{Ce}^{4+}4f$. The Stokes shift is the sum of the large reorganization energies of the Ce^{4+} and Ce^{3+} centers formed after the electron transfer. It equals the energy of the IVCT absorption, which is predicted to exist in this material and to be slightly larger than 10000 cm^{-1} . The large band width is the consequence of the large offset between the minima of the $\text{Ce}^{3+}\text{-Ce}^{4+}$ and $\text{Ce}^{4+}\text{-Ce}^{3+}$ pairs along

the electron transfer reaction coordinate, which is approximately $2\sqrt{3}$ times the difference of Ce-Cl equilibrium distances in the Ce^{3+} and Ce^{4+} centers.

We have shown that the energies of the peaks and the widths of IVCT absorption and emission bands can be calculated *ab initio* with reasonable accuracy from diabatic energy surfaces of the ground and excited states and that these can be obtained, in turn, from independent *ab initio* calculations on the donor and acceptor active centers.

We obtained the energies of the Ce^{3+} and Ce^{4+} active centers of Ce-doped $\text{Cs}_2\text{LiLuCl}_6$ by means of state-of-the-art SA-CASSCF/MS-CASPT2/RASSISO *ab initio* spin-orbit coupling DKH relativistic calculations on the donor cluster $(\text{CeCl}_6\text{Li}_6\text{Cs}_8)^{11+}$ and the acceptor cluster $(\text{CeCl}_6\text{Li}_6\text{Cs}_8)^{12+}$ embedded in an AIMP quantum mechanical embedding potential of the host elpasolite $\text{Cs}_2\text{LiLuCl}_6$. The calculations provide interpretations of unexplained experimental observations in Ce-doped $\text{Cs}_2\text{LiLuCl}_6$ as due to higher energy IVCT absorptions. They also allow to reinterpret other observations. The existence of another IVCT emission of lower energy, at around $14000\text{-}16000 \text{ cm}^{-1}$ less than the $5dt_{2g} \rightarrow 4f$ emission, is also predicted.

IVCT emissions and high energy IVCT absorptions like the ones reported here for $\text{Ce}^{3+}\text{-Ce}^{4+}$ pairs, which are an extension of the known IVCT absorption of mixed-valence compounds, have also been found in Yb-doped solids and are reported separately. They are very likely to exist also in Eu-doped solids and in solids with f-elements in which several valence states can coexist.

Acknowledgments

This work was partly supported by a grant from Ministerio de Economía y Competitividad, Spain (Dirección General de Investigación y Gestión del Plan Nacional de I+D+I, MAT2011-24586).

¹ J. W. Verhoeven, *Pure Appl. Chem.* **68**, 2223 (1996).

² The term IVCT is used sometimes for MMCT between non-equivalent metal ions and also for electron transfer processes not involving metals; here we will adopt the conventional meaning and we will call IVCT only to the homonuclear, symmetric MMCT.

³ R. A. Marcus, *Annu. Rev. Phys. Chem.* **15**, 155 (1964).

⁴ G. C. Allen and N. S. Hush, *Prog. Inorg. Chem.* **8**, 357 (1967).

⁵ M. Robin and P. Day, *Adv. Inorg. Chem. Radiochem.* **10**, 247 (1968).

⁶ A. Werner, *Z. Anorg. Chem.* **12**, 46 (1896).

⁷ N. S. Hush, *Prog. Inorg. Chem.* **8**, 391 (1967).

⁸ N. S. Hush, *Coord. Chem. Rev.* **64**, 135 (1985).

⁹ S. B. Piepho, E. R. Krausz, and P. N. Schatz, *J. Amer. Chem. Soc.* **100**, 2996 (1975).

¹⁰ G. Blasse, *Struct. Bond.* **76**, 153 (1991).

¹¹ P. Boutinaud, R. Mahiou, E. Cavalli, and M. Bettinelli, *J. Lumin.* **122-123**, 430 (2007).

¹² W. van Schaik, S. Lizzo, W. Smit, and G. Blasse, *J. Electrochem. Soc.* **140**, 216 (1993).

¹³ Z. Barandiarán and L. Seijo, "Intervalence Charge Transfer Luminescence: Interplay Between Anomalous and 5d-4f emissions in Yb-doped fluorite-type crystals," *J. Chem. Phys.*, accepted.

¹⁴ A. Bessière, P. Dorenbos, C. van Eijk, K. Krämer, H. Güdel, and A. Galtayries, *J. Lumin.* **117**, 187 (2006).

¹⁵ P. Dorenbos, E. van Loef, C. van Eijk, K. Krämer, and H. Güdel, *Phys. Rev. B* **68**, 125108 (2003).

¹⁶ A. Bessière, P. Dorenbos, C. van Eijk, L. Pidol, K. Krämer, and H. Güdel, *J. Phys.: Condens. Matter* **16**, 1887 (2004).

¹⁷ C.-K. Duan, P. A. Tanner, A. Meijerink, and V. Babin, *J. Phys.: Condens. Matter* **21**, 395501 (2009).

¹⁸ C.-K. Duan, P. A. Tanner, V. Makhov, and N. Khaidukov, *J. Phys. Chem. A* **115**, 8870 (2011).

¹⁹ R. McWeeny, *Proc. R. Soc. Lond. A* **253**, 242 (1959).

²⁰ R. McWeeny, *Methods of molecular quantum mechanics* (Aca-

- demic Press, London, 1989), 2nd ed.
- ²¹ G. Karlström, R. Lindh, P. A. Malmqvist, B. O. Roos, U. Ryde, V. Veryazov, P. O. Widmark, M. Cossi, B. Schimmelpfennig, P. Neogrady, et al., *Comput. Mater. Sci.* **28**, 222 (2003).
- ²² M. Douglas and N. M. Kroll, *Ann. Phys. (N.Y.)* **82**, 89 (1974).
- ²³ B. A. Hess, *Phys. Rev. A* **33**, 3742 (1986).
- ²⁴ B. O. Roos, P. R. Taylor, and P. E. M. Siegbahn, *Chem. Phys.* **48**, 157 (1980).
- ²⁵ P. E. M. Siegbahn, A. Heiberg, B. O. Roos, and B. Levy, *Phys. Scr.* **21**, 323 (1980).
- ²⁶ P. E. M. Siegbahn, A. Heiberg, J. Almlöf, and B. O. Roos, *J. Chem. Phys.* **74**, 2384 (1981).
- ²⁷ K. Andersson, P.-A. Malmqvist, B. O. Roos, A. J. Sadlej, and K. Wolinski, *J. Phys. Chem.* **94**, 5483 (1990).
- ²⁸ K. Andersson, P.-A. Malmqvist, and B. O. Roos, *J. Chem. Phys.* **96**, 1218 (1992).
- ²⁹ A. Zaitsevskii and J.-P. Malrieu, *Chem. Phys. Lett.* **233**, 597 (1995).
- ³⁰ J. Finley, P.-A. Malmqvist, B. O. Roos, and L. Serrano-Andrés, *Chem. Phys. Lett.* **288**, 299 (1998).
- ³¹ G. Ghigo, B. O. Roos, and P.-Å. Malmqvist, *Chem. Phys. Lett.* **396**, 142 (2004).
- ³² B. A. Hess, C. M. Marian, U. Wahlgren, and O. Gropen, *Chem. Phys. Lett.* **251**, 365 (1996).
- ³³ R. Llusar, M. Casarrubios, Z. Barandiarán, and L. Seijo, *J. Chem. Phys.* **105**, 5321 (1996).
- ³⁴ P. A. Malmqvist, B. O. Roos, and B. Schimmelpfennig, *Chem. Phys. Lett.* **357**, 230 (2002).
- ³⁵ J. Paulovic, T. Nakajima, K. Hirao, R. Lindh, , and P.-A. Malmqvist, *J. Chem. Phys.* **119**, 798 (2003).
- ³⁶ B. O. Roos, R. Lindh, P. A. Malmqvist, V. Veryazov, and P. O. Widmark, *J. Chem. Phys.* **112**, 11431 (2008).
- ³⁷ B. O. Roos, R. Lindh, P. A. Malmqvist, V. Veryazov, and P. O. Widmark, *J. Phys. Chem. A* **108**, 2851 (2005).
- ³⁸ B. O. Roos, V. Veryazov, and P. O. Widmark, *Theor. Chim. Acta* **111**, 345 (2003).
- ³⁹ S. Huzinaga, L. Seijo, Z. Barandiarán, and M. Klobukowski, *J. Chem. Phys.* **86**, 2132 (1987).
- ⁴⁰ Z. Barandiarán and L. Seijo, *J. Chem. Phys.* **89**, 5739 (1988).
- ⁴¹ A. Gellé and M.-B. Lepetit, *J. Chem. Phys.* **128**, 244716 (2008).
- ⁴² P. P. Ewald, *Ann. Phys.* **369**, 253 (1921).
- ⁴³ G. Meyer, S. J. Hwu, and J. D. Corbett, *Z. Anorg. Allg. Chem.* **535**, 208 (1986).
- ⁴⁴ L. Seijo and Z. Barandiarán, *J. Chem. Phys.* **94**, 8158 (1991).
- ⁴⁵ Detailed embedding AIMP data libraries in electronic format are available from the authors upon request or directly at the address <http://www.uam.es/quimica/aimp/Data/AIMPLibs.html>. See also Ref. 21.
- ⁴⁶ I. B. Bersuker, *The Jahn-Teller Effect and Vibronic Interactions in Modern Chemistry* (Plenum Press, New York and London, 1984).
- ⁴⁷ P. A. Tanner, C. S. K. Mak, N. M. Edelstein, K. M. Murdoch, G. Liu, J. Huang, L. Seijo, , and Z. Barandiarán, *J. Amer. Chem. Soc.* **125**, 13225 (2003).
- ⁴⁸ B. Ordejón, L. Seijo, and Z. Barandiarán, *J. Chem. Phys.* **126**, 194712 (2007).
- ⁴⁹ G. Sánchez-Sanz, L. Seijo, and Z. Barandiarán, *J. Chem. Phys.* **133**, 114509 (2010).
- ⁵⁰ E. J. Heller, *J. Chem. Phys.* **62**, 1544 (1975).
- ⁵¹ E. J. Heller, *Acc. Chem. Res.* **14**, 368 (1981).
- ⁵² J. I. Zink and K. S. Shin, in *Advances in Photochemistry* (Wiley, New York, 1991), vol. 16, pp. 119–214.
- ⁵³ D. S. McClure and C. Pédrini, *Phys. Rev. B* **32**, 8465 (1985).
- ⁵⁴ B. Moine, B. Courtois and C. Pédrini, *J. Phys. France* **50**, 2105 (1989).
- ⁵⁵ P. Dorenbos, *J. Phys.: Condens. Matter* **15**, 2645 (2003).
- ⁵⁶ J. Gracia, L. Seijo, Z. Barandiarán, D. Curulla, H. Niemansverdriet, and W. van Gennip, *J. Lumin.* **128**, 1248 (2008).

VI. ADDITIONAL MATERIAL

TABLE IV: Computed absorption and emission oscillator strengths of the Ce³⁺ active center in Ce-doped Cs₂LiLuCl₆.

Configuration	State	$f_{abs}(1\Gamma_{7u} \rightarrow)$	$f_{em}(1\Gamma_{8g} \rightarrow)$	$f_{em}(2\Gamma_{8g} \rightarrow)$	$f_{em}(1\Gamma_{6g} \rightarrow)$
$4f^1$	$1\Gamma_{7u}(^2A_{2u})$		1.08×10^{-2}	2.14×10^{-3}	0
	$1\Gamma_{8u}(^2T_{2u})$		1.67×10^{-2}	2.74×10^{-2}	3.29×10^{-5}
	$2\Gamma_{7u}(^2T_{2u})$		1.62×10^{-4}	3.31×10^{-3}	0
	$2\Gamma_{8u}(^2T_{1u})$		5.79×10^{-3}	2.67×10^{-2}	2.60×10^{-5}
	$1\Gamma_{6u}(^2T_{1u})$		5.33×10^{-3}	2.23×10^{-2}	2.86×10^{-5}
$5d_{2g}^1$	$1\Gamma_{8g}(^2T_{2g})$	2.15×10^{-2}			
	$1\Gamma_{7g}(^2T_{2g})$	1.54×10^{-4}			
$5de_g^1$	$2\Gamma_{8g}(^2E_g)$	4.28×10^{-3}			
ITE- a_{1g}^1					
	$1\Gamma_{6g}(^2A_{1g})$	0			

TABLE V: Absorption and emission horizontal offsets of the Ce³⁺–Ce⁴⁺ pair in Cs₂LiLuCl₆, $\Delta Q = Q_{e,f} - Q_{e,i}$, in Å. In Ce³⁺ regular transitions, $\Delta Q = \sqrt{6}(d_{\text{Ce-Cl},e,f} - d_{\text{Ce-Cl},e,i})$. In IVCT transitions, Eq. 11 is used for $Q_{e,f}$ and $Q_{e,i}$, using activated complex, and equilibrium Ce-Cl bond lengths of the left and right clusters from Table III. These values are approximately equal to $\sqrt{3}(\Delta d_R - \Delta d_L)$, Δd_R and Δd_L being the Ce-Cl bond length changes experienced by the Ce⁴⁺ acceptor center (right) and the Ce³⁺ donor center (left) in the IVCT transition.

Branch	Initial state [Ce ³⁺ , Ce ⁴⁺]: Final state	4f absorption [1Γ _{7u} (² A _{2u}), A _{1g}] →	5dt _{2g} emission [1Γ _{8g} (² T _{2g}), A _{1g}] →	5de _g emission [2Γ _{8g} (² E _g), A _{1g}] →	a _{1g} ITE emission [1Γ _{6g} (² A _{1g}), A _{1g}] →
A	[Ce ³⁺ (4f ¹), Ce ⁴⁺]	Ce ³⁺ 4f → 4f	(2) Ce ³⁺ 5dt _{2g} → 4f	(4) Ce ³⁺ 5de _g → 4f	(6) Ce ³⁺ ITE-a _{1g} → 4f
	→ [1Γ _{7u} (² A _{2u}), A _{1g}]	0	+0.103	-0.022	+0.257
	→ [1Γ _{8u} (² T _{2u}), A _{1g}]	+0.005	+0.108	-0.017	+0.262
	→ [2Γ _{7u} (² T _{2u}), A _{1g}]	+0.000	+0.103	-0.022	+0.257
	→ [2Γ _{8u} (² T _{1u}), A _{1g}]	+0.005	+0.108	-0.017	+0.262
	→ [1Γ _{6u} (² T _{1u}), A _{1g}]	+0.007	+0.110	-0.015	+0.265
A [^] _{et}	[Ce ⁴⁺ , Ce ³⁺ (4f ¹)] _{sts}	Ce ³⁺ 4f → Ce ⁴⁺ 4f	Ce ³⁺ 5dt _{2g} → Ce ⁴⁺ 4f	Ce ³⁺ 5de _g → Ce ⁴⁺ 4f	(10)
	→ [A _{1g} , 1Γ _{7u} (² A _{2u})]	0.409	0.343	0.425	
	→ [A _{1g} , 1Γ _{8u} (² T _{2u})]	0.412	0.348	0.428	
	→ [A _{1g} , 2Γ _{7u} (² T _{2u})]	0.409	0.343	0.425	
	→ [A _{1g} , 2Γ _{8u} (² T _{1u})]	0.412	0.348	0.428	
	→ [A _{1g} , 1Γ _{6u} (² T _{1u})]	0.414	0.350	0.430	
B	[Ce ³⁺ (5dt _{2g} ¹), Ce ⁴⁺]	Ce ³⁺ 4f → 5dt _{2g}	(8)		
	→ [1Γ _{8g} (² T _{2g}), A _{1g}]	-0.103			
	→ [1Γ _{7g} (² T _{2g}), A _{1g}]	-0.103			
B [^] _{et}	[Ce ⁴⁺ , Ce ³⁺ (5dt _{2g} ¹)] _{sts}	Ce ³⁺ 4f → Ce ⁴⁺ 5dt _{2g}	(3)		
	→ [A _{1g} , 1Γ _{8g} (² T _{2g})]	0.343			
	→ [A _{1g} , 1Γ _{7g} (² T _{2g})]	0.343			
C	[Ce ³⁺ (5de _g ¹), Ce ⁴⁺]	Ce ³⁺ 4f → 5de _g	(9)		
	→ [2Γ _{8g} (² E _g), A _{1g}]	+0.022			
C [^] _{et}	[Ce ⁴⁺ , Ce ³⁺ (5de _g ¹)] _{sts}	Ce ³⁺ 4f → Ce ⁴⁺ 5de _g	(5)		
	→ [A _{1g} , 2Γ _{8g} (² E _g)]	0.425			
D	[Ce ³⁺ (ITE-a _{1g} ¹), Ce ⁴⁺]	Ce ³⁺ 4f → ITE-a _{1g}			
	→ [1Γ _{6g} (² A _{1g}), A _{1g}]	-0.257			
D [^] _{et}	[Ce ⁴⁺ , Ce ³⁺ (ITE-a _{1g} ¹)] _{sts}				
	→ [A _{1g} , 1Γ _{6g} (² A _{1g})]	0.291			

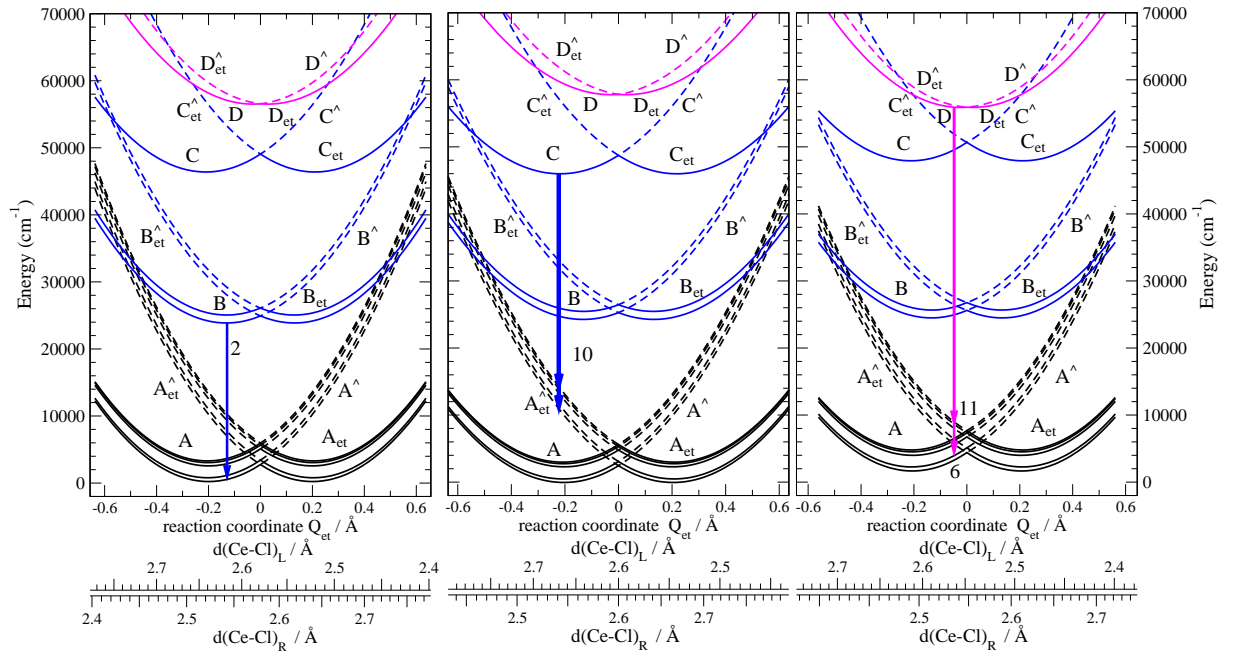


FIG. 7: Energy diagrams of the $\text{Ce}^{3+}\text{-Ce}^{4+}$ pair: Total energies of the $(\text{CeCl}_6)^{3-}\text{-}(\text{CeCl}_6)^{2-}$ cluster pair embedded in $\text{Cs}_2\text{LiLuCl}_6$ vs. the electron transfer reaction coordinates of the $5d$ states $[1\Gamma_{8g}(t_{2g}),A_{1g}]$ (left panel) and $[2\Gamma_{8g}(e_g),A_{1g}]$ (middle panel), and of the impurity-trapped exciton state $[1\Gamma_{6g}(a_{1g}),A_{1g}]$ (right panel). The Ce-Cl distances of the corresponding activated complexes are 2.578 Å, 2.600 Å, and 2.548 Å respectively. Spin-orbit coupling RASSI calculations in the zero electronic coupling limit. Energy scale relative to the ground state energy at equilibrium. See text for a description of the labels.

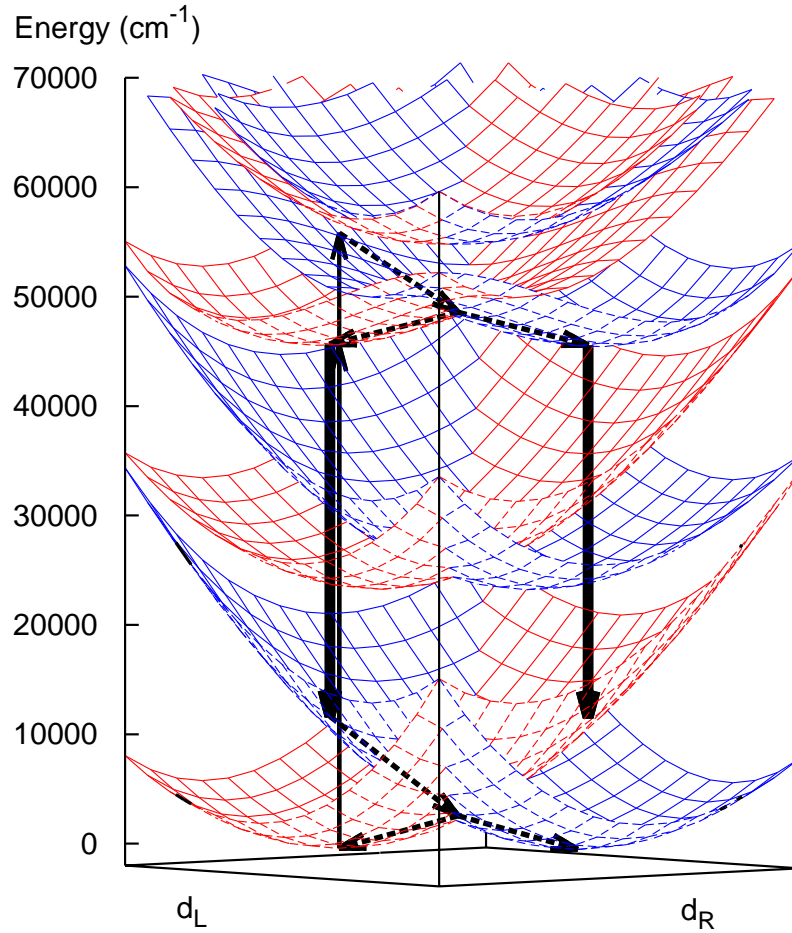


FIG. 8: Anomalous emission in Ce-doped $\text{Cs}_2\text{LiLuCl}_6$ (thick down arrows) interpreted as a $\text{Ce}^{3+}5d_{e_g} \rightarrow \text{Ce}^{4+}4f$ IVCT luminescence taking place between the equilibrium structure of $[\text{Ce}^{3+}(5d_{e_g}^1), \text{Ce}^{4+}]$ and the stressed structure of $[\text{Ce}^{4+}, \text{Ce}^{3+}(4f^1)]$. Excitations of the IVCT luminescence with a $\text{Ce}^{3+}4f \rightarrow 5d_{e_g}$ absorption and a $\text{Ce}^{3+}4f \rightarrow \text{Ce}^{4+}5d_{e_g}$ IVCT absorption are shown with thin up arrows followed by dashed arrows. Nuclei reorganization around the Ce^{4+} and Ce^{3+} centers after the IVCT luminescence is shown with dashed arrows on the lowest energy surfaces. d_R and d_L stand for the Ce-Cl distances in the left and right Ce centers, which are, respectively, Ce^{3+} and Ce^{4+} in the red energy surfaces, and Ce^{4+} and Ce^{3+} in the blue surfaces.